Cloud-radiation interactions and their contributions to convective self-aggregation

Pope, K. N., Holloway, C. E. ORCID: https://orcid.org/0000-0001-9903-8989, Jones, T. R. ORCID: https://orcid.org/0000-0002-7669-1499 and Stein, T. H. M. ORCID: https://orcid.org/0000-0002-9215-5397 (2021) Cloud-radiation interactions and their contributions to convective self-aggregation. Journal of Advances in Modeling Earth Systems, 13 (9). e2021MS002535. ISSN 1942-2466 doi: 10.1029/2021MS002535 Available at https://centaur.reading.ac.uk/100209/

To link to this article DOI: http://dx.doi.org/10.1029/2021MS002535

Publisher: American Geophysical Union

JAMES | Journal of Advances in Modeling Earth Systems®

RESEARCH ARTICLE
10.1029/2021MS002535

Special Section:
Using radiative-convective equilibrium to understand convective organization, clouds, and tropical climate

Key Points:

- The normalized FMSE variance budget is a consistent framework to study aggregation at all SSTs
- Longwave interactions with high clouds and shortwave interactions with moisture affect FMSE variance
- Longwave feedbacks contribute less to aggregation as SST increases as high cloud fraction decreases

Supporting Information:

Supporting Information may be found in the online version of this article.

Correspondence to:
K. N. Pope,
k.n.pope@pgr.reading.ac.uk

Citation:
Pope, K. N., Holloway, C. E., Jones, T. R., & Stein, T. H. M. (2021). Cloud-radiation interactions and their contributions to convective self-aggregation. *Journal of Advances in Modeling Earth Systems*, *13*, e2021MS002535. https://doi.org/10.1029/2021MS002535

Received 8 MAR 2021
Accepted 3 SEP 2021

Cloud-Radiation Interactions and Their Contributions to Convective Self-Aggregation

Kieran N. Pope[1], Christopher E. Holloway[1], Todd R. Jones[1], and Thorwald H. M. Stein[1]

[1]Department of Meteorology, University of Reading, Reading, UK

Abstract This study investigates the direct radiative-convective processes that drive and maintain aggregation within convection-permitting elongated channel (and smaller square) simulations of the UK Met Office Unified Model. Our simulations are configured using three fixed sea surface temperatures (SSTs) following the Radiative-Convective Equilibrium Model Intercomparison Project (RCEMIP) protocol. By defining cloud types based on the profile of condensed water, we study the importance of radiative interactions with each cloud type to aggregation. We eliminate the SST dependence of the vertically integrated frozen moist static energy (FMSE) variance budget framework by normalizing FMSE between hypothetical upper and lower limits based on SST. The elongated channel simulations reach similar degrees of aggregation across SSTs, despite shortwave and longwave interactions with FMSE contributing less to aggregation as SST increases. High-cloud longwave interactions are the main drivers and maintainers of aggregation. Their influence decreases with SST as high clouds become less abundant. This SST dependence is consistent with changes in grid spacing and the critical humidity threshold for condensation (RHcrit). However, the domain-mean longwave-FMSE feedback would likely decrease as grid spacing and RHcrit are reduced by lowering the condensed water path and cloud top height of high-cloud, and altering the distribution of different cloud types. Shortwave interactions with water vapor are key maintainers of aggregation and are dependent on SST and the degree of aggregation itself. The analysis method used provides a new framework to compare the effects of radiative-convective processes on self-aggregation across different SSTs and model configurations to help improve our understanding of self-aggregation.

Plain Language Summary The spontaneous clustering of rainstorms (termed convective self-aggregation) is a common feature in weather and climate models. The amount of aggregation has a large influence on both weather and climate, so being able to understand how aggregation develops and how it is affected by a warming climate is important in both weather and climate modeling. Previous studies have shown that interactions between convection and radiation (both solar radiation and thermal radiation) are crucial for driving and maintaining aggregation. This study provides a detailed analysis of the key radiative-convective interactions that influence aggregation within simulations of the Met Office Unified Model. We assess their sensitivities to the model's sea surface temperature (SST), grid spacing, and critical humidity for cloud formation. We find that the contribution of radiative-convective interactions to aggregation decreases as the SST is increased because the amount of high cloud decreases, and because the difference in absorption of solar radiation between humid and dry regions becomes less significant for aggregation. Decreasing both the model grid spacing, and the model's critical humidity for cloud formation has the effect of decreasing the magnitude of the cloud interactions with thermal radiation, leading to a hypothesized slowing of the rate of aggregation.

1. Introduction

Weather over the tropical oceans is dominated by convection. The tropical atmosphere is in an approximate equilibrium between atmospheric radiative cooling and convective heating called radiative-convective equilibrium (RCE) (e.g., Arakawa & Schubert, 1974). With radiative cooling of the free troposphere, consistently high surface temperatures, and an abundant supply of moisture, convection occurs in an attempt to neutralize conditional instability, resulting in strong rainstorms. This convection can form a wide variety of structures with a great range of spatial and temporal scales depending on the state of convective organization. Structures can range from individual cumulonimbus clouds, to squall lines, mesoscale convective systems

(MCSs), tropical cyclones, and the Madden-Julian Oscillation (MJO) (Houze, 2004; Madden & Julian, 1971; Mapes & Houze, 1993; Nakazawa, 1988). The degree of aggregation affects the environment of both the convective and surrounding subsiding regions (Wing, 2019), as well as global-scale circulations (Arnold & Randall, 2015) and climate (Coppin & Bony, 2018).

There are many processes that cause convective organization, including convection within equatorial waves (Kiladis et al., 2009), organization along fronts, SST hotspots, land, and orography. Another process has been termed convective self-aggregation: a process, first identified in idealized models, by which convection spontaneously becomes clustered despite homogeneous initial conditions and forcing (e.g., Wing et al., 2017).

Self-aggregation has been the focus of many recent studies, the majority of which have used idealized simulations of RCE to further understand the processes that cause this phenomenon (Bretherton et al., 2005; Held et al., 1993; Muller & Held, 2012; Wing & Emanuel, 2014). Self-aggregation has important consequences for weather and climate, with aggregation leading to a reduction in high cloud fraction and domain-mean humidity, leading to an increase in atmospheric radiative cooling (Wing et al., 2020). Extreme instantaneous precipitation rates are largely unaffected by aggregation, but extreme daily precipitation rates increase with self-aggregation thanks to the increased clustering of rainstorms and enhanced precipitation efficiency (Bao & Sherwood, 2019). A review of self-aggregation in numerical models has been published by Wing et al. (2017). Despite self-aggregation being first recognized in these idealized numerical models, key processes that drive self-aggregation are indeed relevant to the real atmosphere (Holloway et al., 2017).

We use the spatial distribution of frozen moist static energy (FMSE) as a framework to study aggregation (Wing & Emanuel, 2014). FMSE, or h, is given by

$$h = c_p T + gz + L_v q_v - L_f q_i \tag{1}$$

where c_p is the specific heat of dry air at constant pressure, T is the temperature, g is the gravitational acceleration, z is the height above the surface, L_v is the latent heat of vapourization, q_v is the water vapor mixing ratio, L_f is the latent heat of fusion, and q_i is the condensed ice mixing ratio.

The density-weighted vertical integral of FMSE is only affected by radiation, surface fluxes, and advection. Under convective processes, FMSE is approximately conserved, though redistributed. As convection becomes more clustered, the horizontal variance in vertically integrated FMSE increases. A budget equation for the rate of change of vertically integrated FMSE shows that the horizontal variance in vertically integrated FMSE is driven by feedbacks with radiation, surface fluxes, and advection. There is some disagreement over the importance of each feedback to aggregation, as well as their SST dependencies and dependencies on aggregation (Wing et al., 2017). The majority of studies find surface flux feedbacks are strong, positive contributors to aggregation at early stages, sometimes being the leading driver of aggregation. However, their SST dependence is up for debate with the feedback either increasing (Coppin & Bony, 2015), decreasing (Becker et al., 2017), or remaining similar with SST (Wing & Cronin, 2016). Feedbacks between FMSE and both shortwave and longwave radiation have been shown to be key drivers and maintainers of aggregation (e.g., Becker et al., 2017; Holloway & Woolnough, 2016; Wing & Cronin, 2016), and interactive radiation in models is essential for aggregation to occur (Bretherton et al., 2005; Muller & Bony, 2015).

Muller and Held (2012) find that it is the longwave cooling effect of low clouds within dry regions that is responsible for the onset of self-aggregation. The resultant circulation driven by the radiative cooling drives an upgradient transport of FMSE, which increases the variance of FMSE. They find the sensitivity of self-aggregation to domain size and resolution to be a result of the sensitivity of low cloud distributions within the model. Once the convection is aggregated, the longwave cooling effect of low clouds is not necessary to maintain aggregation (Muller & Bony, 2015; Muller & Held, 2012). During the mature phase of aggregation, the reduced longwave cooling of high clouds within high-FMSE regions becomes the dominant feedback maintaining aggregation (Wing & Emanuel, 2014).

Wing and Emanuel (2014) note the importance of the shortwave radiative feedback due to the increased absorption of shortwave radiation within high FMSE regions compared to low FMSE regions, increasing the FMSE variance. Although this feedback has a small effect compared to the longwave feedback during the early and mature stages of aggregation, they find it dominates the total radiative feedback at the intermediate stage. They also note that dry regions initially have anomalously strong radiative cooling, resulting in a positive longwave feedback, whereas at later times, the dry regions amplify, becoming dryer, which decreases low-level emissivity. Anomalous longwave heating then develops at low levels to the extent that the column longwave heating anomaly becomes positive.

Some studies have analyzed the role of cloud on the radiative feedbacks by comparing the clear-sky radiative fluxes to the total radiative fluxes (e.g., Wing & Emanuel, 2014; Wing & Cronin, 2016). The contributions from cloud-radiation interactions to convective self-aggregation have been generally shown to be important in previous studies, but a detailed analysis considering the role of specific cloud types is missing. With both the horizontal and vertical distribution of clouds being one of the largest sources of variability amongst RCE simulations (Wing et al., 2020), a detailed investigation into the role of specific cloud types on self-aggregation may help in explaining the variability of self-aggregation amongst RCE simulations and the consequential implications for climate sensitivity.

This study investigates the direct radiative-convective processes that are important to self-aggregation, and their sensitivity to SST within elongated channel simulations of the UK Met Office Unified Model (UM) version 11.0. We then investigate how the SST-dependent convective features and their radiative interactions are affected by model grid spacing and treatment of subgrid condensation using smaller square domains. Our simulations are configured using three fixed SSTs following the Radiative-Convective Equilibrium Model Intercomparison Project (RCEMIP) protocol. The model setup is described in Section 2.1. We use a budget equation for the variance of normalized vertically integrated FMSE which minimizes the SST dependence of horizontal FMSE variance (Section 2.2). This allows us to compare how the impacts of radiative feedbacks on aggregation change with SST. We categorize cloud types based on the vertical distribution of condensed water path (CWP) and analyze their radiative interactions that impact aggregation. This categorization is shown in Section 2.3.

We first analyze how convection aggregates within the three channel simulations in Section 3, and show how the FMSE budget terms vary with time and SST. We then analyze the radiative feedbacks responsible for maintaining aggregation in the large domain and compare how SST affects these feedbacks in Section 4. Then, we look at the dominant radiative feedbacks during the early stages of aggregation and see how they change with time (Section 5). Finally, we investigate how these radiative interactions are affected by both resolution and the critical humidity threshold for condensation to occur (RHcrit), using smaller domains with lower grid spacing (Section 6). A summary and conclusions are presented in Section 7.

2. Methods

2.1. Model Configuration

In this study, we use the UK Met Office Unified Model version 11.0 to simulate RCE at three fixed SSTs: 295, 300, and 305 K. This study mainly focuses on convection within the "*LARGE*" domain; a 6,048 km 432 km elongated channel domain with a 3 km horizontal grid spacing. However, we also use three smaller 100 km × 100 km domains: "*SMALL*" (1 km grid spacing), "*SMALL_RHCRIT*" (1 km grid spacing), and "*SMALL_HI*" (0.1 km grid spacing), to assess how the radiative properties of clouds are affected by the critical humidity threshold for condensation (RHcrit) and grid spacing.

The *LARGE*, *SMALL*, and *SMALL_RHCRIT* simulations have been configured following the RCEMIP protocol set out by Wing et al. (2018). The *SMALL_HI* domain only differs from this protocol in that the horizontal grid spacing is 10 times finer than the other 100 km × 100 km simulations in RCEMIP. The *LARGE* and *SMALL* simulations have been submitted to RCEMIP under the model name "UKMOi-vn11.0-RA1-T," with the name "UKMO-RA1-T" being used in subsequent RCEMIP comparison papers (Becker & Wing, 2020; Wing et al., 2020).

RHcrit is a parameter in the Smith sub-grid cloud scheme (Smith, 1990) used in our models, and is the grid-box mean relative humidity at which sub-grid humidity fluctuations are assumed large enough to result in some fraction of the grid-box becoming saturated and forming cloud. The *LARGE*, *SMALL*, and *SMALL_HI* simulations all have a uniform RHcrit value of 0.99 across the entire domain. The value of RHcrit should depend on the dimensions of the grid-box, with coarser grid-boxes requiring a lower RHcrit to yield realistic cloud amounts. Our value of 99% is too high to yield realistic low cloud distributions (Morcrette, 2013) including at km-scale grid spacings. To see the effects of a more realistic RHcrit, we used another set of simulations that are identical to our *SMALL* simulations but for an RHcrit distribution used in the UK Met Office UKV model. Here, RHcrit is set to 96% in the lowest layers and decreases steadily to 80% at 900 m. RHcrit is then maintained at 80% above this level.

The RCEMIP protocol states that large-domain simulations for a given SST are initialized using the equilibrium soundings of the corresponding small-domain simulations, providing aggregation does not occur in the small-domain. In our case, the *SMALL* simulations showed signs of self-aggregation, therefore, our *LARGE* simulations are initialized from a corresponding small-domain simulation with homogenized radiation, which showed no sign of aggregation. Note that there was a mistake in the initialization of the *LARGE* simulations, in that the initial humidity profile is out by a density factor. Since density is close to unity in the lower troposphere, this mistake does not result in supersaturation at any level, and only results in the upper troposphere being drier than it should. Within 2 days of the simulation, convection remoistens the upper troposphere to a similar level to the intended initial profile. With the 2-day spin-up period neglected in the conclusions of our analysis, we believe this error will not have an impact on our conclusions.

The simulations are configured over an ocean, without rotation, and have a fixed solar insolation of 409.6 W m^{-2} (the tropical annual mean). The *LARGE* domain simulations are run for 113 days, the *SMALL* simulations are 124 days, the *SMALL_HI* simulations are 54 days, and the *SMALL_RHCRIT* simulations are 123 days 3D data are produced every 6 h, which is the temporal resolution of our analysis.

The science configuration of our simulations is based on the tropical Regional Atmosphere and Land (RAL1-T) configuration (Bush et al., 2020). However, we use the Smith sub-grid cloud scheme (Smith, 1990) rather than the PC2 scheme (Wilson et al., 2008). With our simulations configured over an ocean, the land settings of RAL1-T are not used. The simulations use explicit convection set over a flat, Cartesian grid, with biperiodic boundary conditions, using a vertical sigma-z-coordinate Charney-Philips staggering (Charney & Phillips, 1953). We use a 60 s time step for the *LARGE* simulations, a 30 s time step for the *SMALL* and *SMALL_RHCRIT* simulations, and a 5 s time step for the *SMALL_HI* simulations. The dynamical core uses a semi-implicit, semi-Lagrangian scheme that solves the non-hydrostatic, fully compressible, deep-atmosphere equations of motion (Wood et al., 2014).

The radiation scheme used is the Suite of Community Radiative Transfer codes based on Edwards and Slingo (SOCRATES) (Edwards & Slingo, 1996) with the full radiation being computed at 15-min time steps and the simplified radiation at 5-min time steps. The boundary layer scheme used is based on that described in Lock et al. (2000) with updates described in Walters et al. (2019). The subgrid turbulence scheme is based on Smagorinsky (1963) with multiple extensions from Lock et al. (2000). We use Rayleigh damping of all prognostics in a "sponge layer" in the upper levels of the model, with the damping timescale following an exponential function of height from 24 to 40 km. The microphysics used is a single-moment scheme based on Wilson and Ballard (1999).

2.2. Normalization of FMSE

Using the variance of vertically integrated FMSE (var($\hat{h}$)) as the metric for comparing aggregation across different SSTs has its pitfalls as it is very strongly dependent on temperature. To account for this, we normalize vertically integrated FMSE between a theoretical upper and lower limit using Equation 2, yielding values of normalized FMSE ($\hat{h}_n$) between 0 and 1.

$$\hat{h}_n = \frac{\hat{h} - \hat{h}_{\mathrm{min}}}{\hat{h}_{\mathrm{max}} - \hat{h}_{\mathrm{min}}} \tag{2}$$

Here, hats (^) denote a density-weighted vertical integral, and $\hat{h}_{\mathrm{max}}$ and $\hat{h}_{\mathrm{min}}$ are upper and lower limits of $\hat{h}$ for a given SST. $\hat{h}_{\mathrm{max}}$ is defined as the vertically integrated FMSE of a fully saturated moist pseudoadiabatic profile from the surface to the tropopause, plus the integrated FMSE of the initial profile for the *LARGE* simulations above the tropopause. For $\hat{h}_{\mathrm{min}}$, the vertically integrated FMSE of a dry adiabatic profile with zero moisture is used within the troposphere, and again, integrated FMSE above the tropopause from the initial profile is added. The SST is used as the temperature at sea-level pressure to initiate both adiabatic

Table 1
Values of $\hat{h}_{max}$ and $\hat{h}_{min}$ for Each SST Used in Equation 2 to Normalize $\hat{h}$

SST (K)	$\hat{h}_{\min}$ (GJm^{-2})	$\hat{h}_{\max}$ (GJm^{-2})	Tropopause pressure (hPa)	Tropopause altitude (km)	$\hat{h}$ above tropopause (GJm^{-2})
295	3.177	3.563	92.0	16.1	0.386
300	3.228	3.753	91.3	16.6	0.387
305	3.272	3.988	80.0	17.9	0.348

profiles. The tropopause is defined as the lowest level in the initial profile at which the lapse rate decreases to 2°C/km or less. The values of $\hat{h}_{\max}$ and $\hat{h}_{\min}$ are shown in Table 1, along with the height and pressure of the tropopause and the integrated FMSE above it. With less than 11% of the mass-weighted integral of $\hat{h}_{\max}$ and $\hat{h}_{\min}$ coming from the FMSE above the tropopause, the way we define the tropopause has little effect on these limits and does not impact our conclusions.

For all of our SSTs, variations in $\hat{h}_n$ are dominated by horizontal variations in moisture. By computing the individual components of $\hat{h}_n$ from the terms in Equation 1, we find the horizontal variance of the thermal energy component of $\hat{h}$ is approximately 0.5% of the variance of the moisture component of $\hat{h}$ for all SSTs. The variances of the geopotential energy and ice content terms are negligible in comparison to the variance of the moisture term. Average anomalies in the moisture component of $\hat{h}$ increase exponentially with SST and are proportional to the difference between $\hat{h}_{\min}$ and $\hat{h}_{\max}$. Therefore, this normalization technique approximately eliminates the SST dependence of var($\hat{h}$).

The relative importance of different processes to changing the variance of FMSE can be analyzed using the budget equation derived by Wing and Emanuel (2014):

$$\frac{1}{2}\frac{\partial \hat{h}'^2}{\partial t} = \hat{h}'LW' + \hat{h}'SW' + \hat{h}'SEF' - \hat{h}'\nabla_h.\widehat{\mathbf{u}h} \tag{3}$$

where SEF is the surface enthalpy flux, made up of the surface latent heat and sensible heat fluxes, $\nabla_h.\widehat{\mathbf{u}h}$ is the horizontal divergence of the $\hat{h}$ flux, primes (′) indicate local anomalies from the instantaneous domain-mean, and LW and SW are the net atmospheric column longwave and shortwave heating rates.

This equation is suitable for comparing the importance of different $\hat{h}$ feedbacks to aggregation within models at the same SST. However, due to the strong dependence of var($\hat{h}$) to SST, this equation cannot be used to analyze how the importance of these feedbacks to aggregation change with SST. To enable fair comparisons of aggregation with SST, we frame our analysis using a budget of the horizontal variance of $\hat{h}_n$. By following the budget equation derivation by Wing and Emanuel (2014) and using $\hat{h}_n$ instead of $\hat{h}$, Equation 3 becomes:

$$\frac{1}{2}\frac{\partial \hat{h}_n'^2}{\partial t} = \hat{h}_n'LW_n' + \hat{h}_n'SW_n' + \hat{h}_n'SEF_n' - \hat{h}_n'\nabla_h.\widehat{\mathbf{u}h_n} \tag{4}$$

Here, each of the three normalized flux anomalies on the RHS (LW_n', SW_n', and SEF_n') is equal to the original flux anomaly in Equation 3 divided by the difference between $\hat{h}_{\max}$ and $\hat{h}_{\min}$. The derivation of this equation is shown in the Appendix A.

In Wing and Emanuel (2014), the budget terms are normalized by the instantaneous FMSE variance, which results in a couple of differences from our method. First, as the variance of FMSE increases, the magnitude of their terms tends to decrease because the terms are divided by a larger value, whereas the terms in Equation 4 tend to increase in magnitude as $\hat{h}_n'$ is a factor in every term. The SST sensitivity of the terms may also be different if the degree of aggregation (as measured by normalized FMSE variance) changes with SST. For example, if aggregation increases with SST, then Wing and Emanuel (2014) would find the magnitude of the budget terms decrease with SST as the terms are divided by a much larger FMSE variance, whereas following Equation 4, $\hat{h}_n'$ would increase and therefore the individual terms increase with SST. If the degree of aggregation is similar across all SSTs as measured by var($\hat{h}_n$) (which is the case in our *LARGE* simulations),

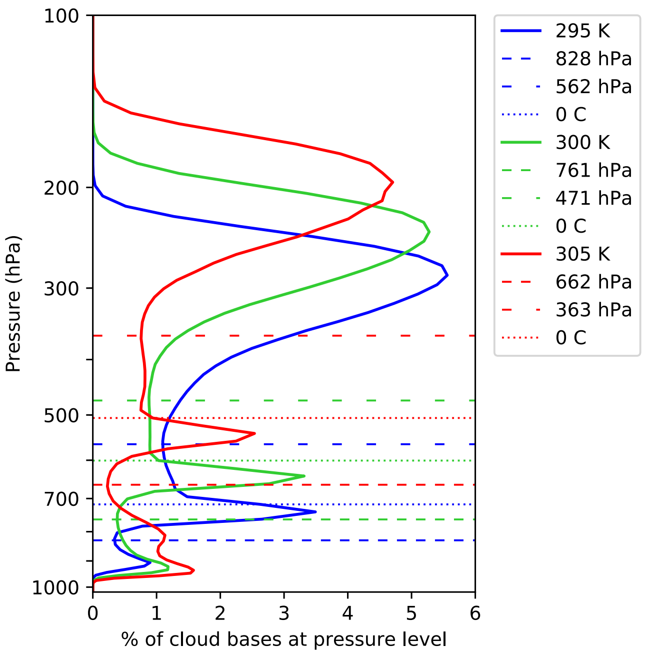

Figure 1. Cloud base distributions throughout each of the *LARGE* domain simulations. The lower and upper pressure thresholds (P1 and P2) for each sea surface temperature are shown in narrow and wide dashed lines, respectively, and the mean freezing level is shown in dotted lines.

then the SST dependence of the budget terms would be very similar during the mature stage of aggregation regardless of which normalization method is used.

2.3. Cloud Classification Scheme

The cloud classification scheme is based on Hill et al. (2018), using the vertical structure of condensed water content to define different cloud types. High-level clouds are defined to be located above an upper-level pressure threshold, low-level clouds are located below a lower-level threshold, and mid-level clouds are anything in between. Clouds spanning two or more levels have their own categories. In this study, a minimum condensed water content of 10^{-6} kg m^{-3} is used as a cloud threshold. This is the approximate limit below which the average difference between the longwave and shortwave heating rates of clear-sky (without condensed water) and total radiative transfer calculations are less than 1 K day^{-1}, and an order of magnitude lower than the value for mean cloud condensed amount (analysis not shown).

We use different high and low cloud pressure level thresholds for each SST to account for the change in depth of the troposphere. The thresholds for a given SST are determined from the average vertical profile of cloud bases throughout the entire *LARGE* domain simulation. Distributions of cloud base pressures for each of the *LARGE* simulations are shown in Figure 1. The cloud base at a given column is calculated as the lowest-altitude pressure at which the condensed water content exceeds 10^{-6} kg m^{-3} (the distribution shown, therefore, does not account for additional cloud bases above the lowest base). The profiles of cloud base have very similar features for each SST, with two consistent local minima within each distribution. These two minima are the chosen pressure thresholds that define the cloud types throughout this study. The lower-level threshold is defined as the first cloud base distribution local minimum below the freezing level. The upper-level threshold is the highest-altitude cloud base distribution local minimum. The lower-level thresholds (P1), and the upper-level thresholds (P2) for each SST are shown in Figure 1.

Rather than using all 12 cloud types used by Hill et al. (2018), we have merged the cloud types that were only distinguishable by whether or not they are vertically contiguous. We analyzed radiative heating rates for all 12 cloud types, and found that the types we have merged have similar heating rates for a given CWP (not shown). The merged cloud types also have similar $\hat{h}$ distributions, meaning they will have similar radiative interactions for a given CWP. The main difference between the individual cloud types is their CWP distributions, with the contiguous types tending to have higher CWPs. We end up with eight cloud types used in this study, including Clear regions. A schematic of the categories is shown in Figure 2.

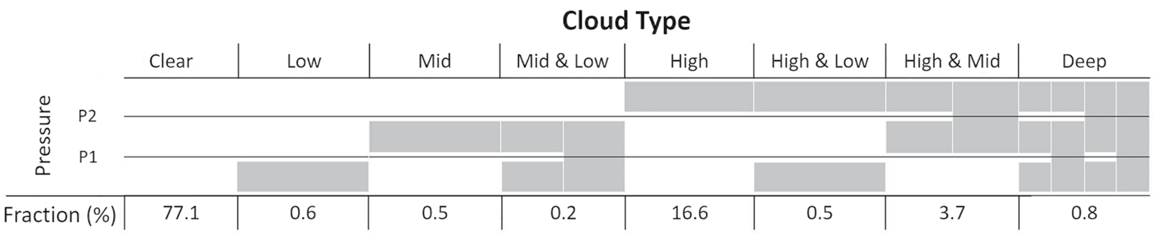

Figure 2. Schematic of the categories used in this study. P1 and P2 are the lower-level and upper-level pressure thresholds, respectively. The shading is contiguous across rows if the cloud type extends across multiple layers. The mean domain fractions for each cloud type throughout the entirety of the *LARGE*, 300 K sea surface temperature (SST) simulation are shown. Note that fractions are sensitive to aggregation and SST.

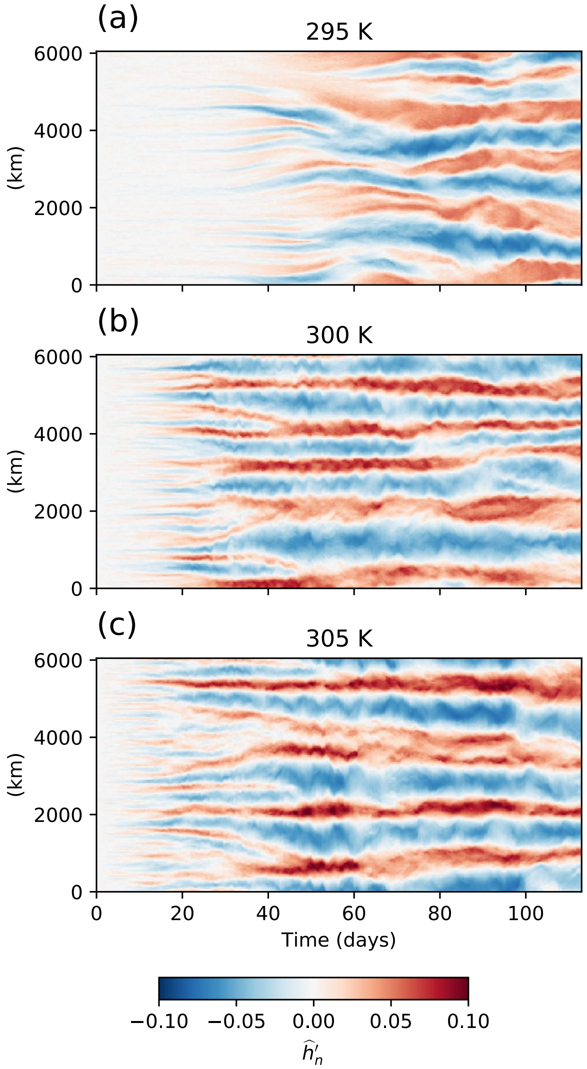

Figure 3. Hovmöller diagrams of $\hat{h}_n$ for each sea surface temperature for the *LARGE* domain runs. $\hat{h}_n$ is averaged across the short axis of the domain.

3. Aggregation Within the *LARGE* Domain

Within the first 5 h of our simulations, convection initiates rapidly and homogeneously, with scattered convection appearing across the entire domain. After a couple of days, dry regions begin to develop within which deep convection is suppressed. These dry regions begin to grow in size and subsequently become drier, reminiscent of the radiatively driven cold pool process described in Coppin and Bony (2015). As the dry regions expand and merge, the moist regions become increasingly confined and become moister. The most prevalent dry regions are usually surrounded by the most intense convection. Dry regions continue to expand, constricting the moist regions until an equilibrium state is reached with quasi-stationary bands of intense convection being separated by dry regions with little cloud. This evolution is consistent with the majority of non-rotating large-domain simulations of RCE (Wing et al., 2017, 2020).

Hovmöller plots for each simulation are shown in Figure 3 using $\hat{h}_n$ as a proxy for moist convective regions. The Hovmöller diagrams were made by averaging $\hat{h}_n$ along the short axis of the domain. The evolution of the variance of column-integrated FMSE for each SST is shown in Figure 4a. Visually, this metric has a strong correlation with SST since a warmer atmosphere is able to contain exponentially more water vapor via the Clausius-Clapeyron relationship, so there is a larger difference in FMSE between the dry and moist regions. Normalization allows for fair comparisons of aggregation across all SSTs whilst using the FMSE variance framework, as shown in Figure 4b. Var($\hat{h}_n$) is a consistent metric for each SST, with values less than 10^{-4} corresponding to uniformly scattered convection, and values greater than 10^{-3} corresponding to strong convective aggregation. Aggregation via this metric reaches a similar level once the convective aggregation is in equilibrium despite convection organizing into four bands in the 305 K simulations and five in the other simulations. We note however that when considering multiple metrics of convective aggregation for these simulations there is no agreement on the SST sensitivity of aggregation in the final equilibrium state. Wing et al. (2020) found that the subsidence fraction and the organization index (I_{org}) both increase with SST for these simulations, indicating that the convection forms into more constricted bands as SST increases, whereas the variance of column relative humidity slightly decreases with SST.

Considering the Hovmöller plots in Figure 3, the fully aggregated state is reached around day 50 for the 300 and 305 K simulations and around day 75 for the 295 K simulation. This difference in aggregation rate can be attributed to the ability of dry regions to expand and amplify. In the 300 and 305 K simulations, the dry patches that form very early on merge, amplify and continue to expand until the equilibrium state is reached. However, in the 295 K simulation, these patches struggle to amplify and are easily remoistened, allowing convection to reoccur in that location—more persistent dry patches begin to develop around day 15 and slowly expand and confine the convection to form the quasi-stationary bands.

The points in time at which the variances of $\hat{h}$ level off in Figure 4 appear to occur earlier than the points in time at which the convection appears fully aggregated in Figure 3 particularly for the 300 and 305 K simulations. This could in part be due to the averaging along the short axis of the domain for the Hovmöller diagrams, smoothing out any features that do not extend across the entire short axis. However, once the moist regions no longer get moister, and the dry regions no longer become drier, var($\hat{h}$) will reach its maximum value. It may only take around the timescale of a convective cell for a column to reach the upper limit of $\hat{h}$, however, it takes much longer for the driest regions to reach the lower limit. The drying of the dry regions

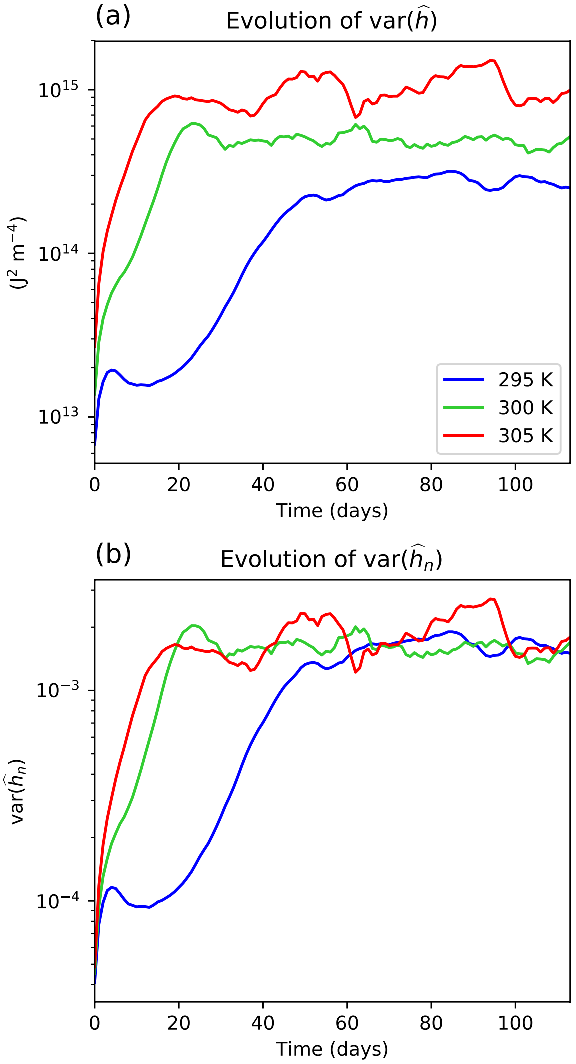

Figure 4. Daily means of the (a) spatial variance of $\hat{h}$ and (b) spatial variance of $\hat{h}_n$, for each sea surface temperature for the *LARGE* domain.

may be on the same timescale as the subsidence timescale; the time it takes for the very dry air near the tropopause to descend throughout the depth of the free troposphere. Var($\hat{h}$) correlates strongly with aggregation, although it does not necessarily indicate how clustered the convection is once the maximum variance is reached. This is not a surprising result. Beucler and Cronin (2019) relate the evolution of the length-scale of convection aggregation to the FMSE budget terms, showing that the processes that increase FMSE variance are not always the processes that increase the length-scale of aggregation. This allows convection to spatially reorganize without changing FMSE variance.

Time series of the domain-mean values of the terms in the $\hat{h}_n'^2$ budget (Equation 4) are shown in Figures 5a–5c. Where the terms are positive, they are contributing to an increase in var($\hat{h}_n$), and hence encourage aggregation (note that the advection term is calculated as a residual of the other terms). Figure 5d shows the mean values of the budget terms for a given degree of aggregation for each SST in terms of var($\hat{h}_n$). From this, the SST dependence of the budget terms can be seen throughout the aggregation process. The growth phase of aggregation can be seen where the var($\hat{h}_n$) tendency is strongly positive (typically where var($\hat{h}_n$) $< 1.4 \times 10^{-3}$, compare with Figure 4b) and the maintenance phase is where the tendency is close to zero. The magnitude of all terms tends to increase as var($\hat{h}_n$) increases since each term in the equation is a product that includes $\hat{h}_n'$.

The longwave feedback is the main driver of aggregation in each of our simulations, with its contribution to aggregation insensitive to SST during the growth phase. Most studies are in agreement that the longwave feedback is a strong positive driver of aggregation, whereas Wing and Cronin (2016) found that the longwave feedback increases with SST. They find that this SST dependence is mainly due to clouds, hypothesizing that since the atmosphere is so optically thin at lower SSTs, the presence of clouds in the moist regions increases radiative cooling by increasing the number of longwave emitters. Specifically, the presence of low clouds would have a larger effect than high clouds as their warm cloud tops would emit more radiation. Our simulations have a distinct lack of low cloud compared to most cloud-resolving models (Wing et al., 2020), and this may be the reason we do not see this trend. We find the longwave feedback is also the dominant maintainer of aggregation, however, its contribution to maintenance falls with SST. This is discussed further in Section 4.1.

The shortwave feedback is always positive and is highly sensitive to SST, with higher SSTs having smaller shortwave feedbacks. Its contribution to driving aggregation is small compared to the longwave term especially for warmer SSTs, though it is roughly three-quarters of the magnitude of the longwave feedback during the maintenance phase. These results are in agreement with Wing and Cronin (2016) and are discussed further in Section 4.3.

A more surprising result is the magnitude of the surface flux feedback which is a strong negative feedback at all stages and SSTs except for the very earliest stages of aggregation. This is in contrast to the majority of studies that find the surface flux feedback to be one of the dominant drivers of aggregation (Wing et al., 2017). Wing and Emanuel (2014) describe two opposing surface flux feedbacks at play. First, surface wind speeds are higher in moister regions resulting in a positive feedback which helps drive aggregation. On the other hand, there is enhanced evaporation in the dry regions due to enhanced air-sea enthalpy disequilibrium resulting in a negative feedback. Typically the former feedback dominates at early stages,

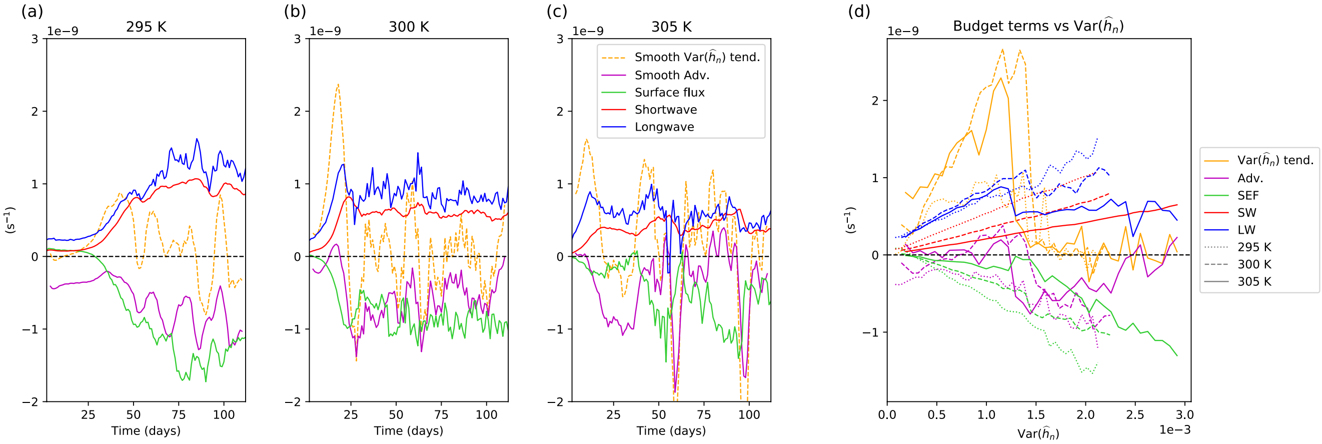

Figure 5. Domain-mean of RHS terms in Equation 4 for (a) 295, (b) 300, and (c) 305 K within the *LARGE* domain. Each point represents a daily mean of the term. The advection term is calculated as a residual of the other terms. Both the var($\hat{h}_n$) tendency and the advection term are 5-day running averages, shown to reduce noise. (d) Mean of each term against var($\hat{h}_n$) calculated for 40 evenly spaced var($\hat{h}_n$) bins.

whereas the latter is more relevant for aggregated convection (Wing et al., 2017). The surface flux feedback is also highly sensitive to SST, with higher SSTs generally having a less negative surface flux feedback. The reasons for the surface flux feedback's sensitivity to aggregation and SST are not investigated in this study.

Figure 5d shows the sum of all the diabatic feedbacks is similar at all stages of aggregation in each of our simulations, however the rate of change of aggregation increases with SST. The reason for the increase is due to the SST sensitivity of the advection term. At early stages of aggregation (var($\hat{h}_n$) $< 0.8 \times 10^{-3}$) the (usually negative) advection feedback becomes increasingly positive as SST increases and is approximately zero for the 305 K simulation. This accelerates the aggregation process for higher SSTs. Muller and Bony (2015) highlight the importance of radiatively driven circulations from low clouds that result in upgradient transport of FMSE resulting in a positive feedback. Despite our simulations having a notable lack of low cloud, the average fraction of low-level cloud increases from 1.4% at 295 K to 3.2% at 305 K, and may be a factor in explaining the SST dependence of the advection term. We do not explore the reason for this relationship further in this study.

There are two occasions in the 305 K simulations in which var($\hat{h}_n$) rapidly decreases. These are between days 55 and 60 and days 95 and 100 (Figure 4). Approximately 5 days before var($\hat{h}_n$) decreasing, the intensity of the convection in the moist bands begins oscillating with a period of 2–5 days. The convection can become so intense that anvil clouds spread far away from the convective updrafts and over the driest regions of the domain. This creates anomalous longwave heating over anomalously dry regions, resulting in a sharp decrease in the domain-mean longwave term (Figure 5c; days 55 and 95). The intense convection might also generate intense circulations that transport high $\hat{h}$ away from moist regions, creating the strongly negative advection feedbacks which ultimately cause var($\hat{h}_n$) to fall. These events are not directly caused by radiation-convection interactions so they are not investigated further in this study.

In Section 4, we discuss radiation-FMSE interactions during the "Mature" phase of aggregation, and we discuss the "Growth" phase of aggregation in Section 5. We define the Mature phase of aggregation to be after the time at which the convection is most clustered (after day 75 for the 295 K simulation, and after day 50 for the 300 and 305 K simulations, following Figure 3) and where var($\hat{h}_n$) is between 1.5×10^{-3} and 2×10^{-3}. This var($\hat{h}_n$) range was chosen because the mean var($\hat{h}_n$) tendency is close to zero for each SST (Figure 5d) and the simulations are within this range for a sizable duration (Figure 4b). Fluctuations in var($\hat{h}_n$) outside this range will not bias the results. The Growth phase is sampled for var($\hat{h}_n$) between 3×10^{-4} and 4×10^{-4}. This is an arbitrary range—using any range in which aggregation increases rapidly for all SSTs does not affect the conclusions of these results. We have chosen these narrow ranges to compare convection at similar stages of aggregation, with FMSE anomalies being similar in magnitude.

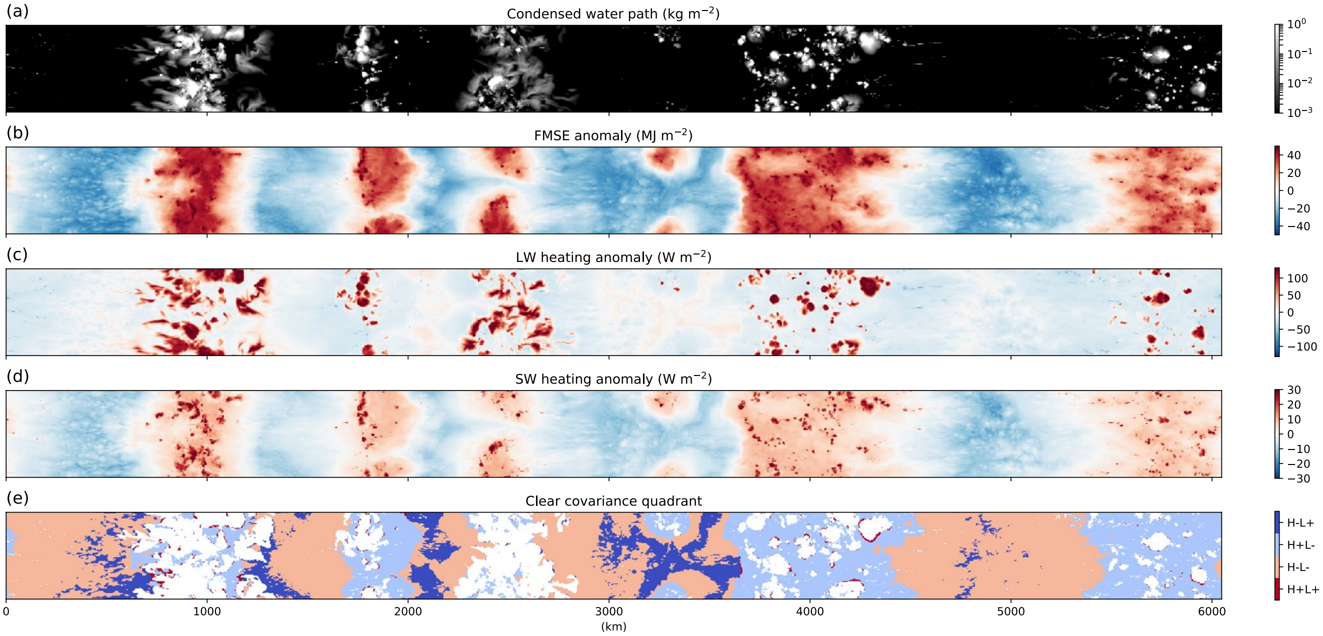

Figure 6. Maps of (a) condensed water path (kg m^{-2}), (b) Frozen moist static energy (FMSE) anomaly (MJ m^{-2}), (c) longwave heating anomaly (W m^{-2}), (d) shortwave heating anomaly (W m^{-2}), (e) Clear covariance quadrant (Section 4.2)—note that clouds are colored white in (e). Snapshots taken at day 100 in the *LARGE* domain with SST = 300 K. Regions where the FMSE anomaly ("H") and radiative heating anomaly ("L") have the same sign contribute to increasing var ($\hat{h}$). Note that the FMSE, shortwave and longwave anomalies are not normalized.

4. Cloud Type Contributions During the Maintenance of Aggregation

Interactions between radiation and cloud/moisture responses to convection have been shown to be crucial contributors to convective self-aggregation (e.g., Arnold & Putman, 2018; Wing et al., 2017). In this section, we investigate the impacts of cloud-radiative interactions on the maintenance of self-aggregation during the Mature phase of aggregation within our *LARGE* simulations. Figures presented in Sections 4.1 and 4.2 also display data for the Growth phase of aggregation which are discussed in Section 5.

Note that the results presented here are limited to our specific simulations. They are outliers in RCEMIP in a number of ways, so the results might not be representative of all RCE simulations. Wing et al. (2020) report that in terms of cloud fraction, our *LARGE* simulations have roughly 5 times less low-level cloud compared to the mean of the other RCEMIP cloud-resolving models, but they also have one of the largest high-cloud fractions.

The radiative heating rate of an atmospheric column is determined by the difference between the radiative fluxes into the atmosphere and the radiative fluxes out. The only longwave flux into the atmosphere is the upwelling surface radiation which is uniform in space and time in our simulations, owing to the fixed SST. Therefore, the longwave heating rate is determined by the magnitudes of the downwelling flux into the surface and the outgoing longwave radiation (OLR). These fluxes are sensitive to the emission heights and opacities of different layers, which in turn depend on the profiles of cloud and moisture. Net longwave radiation into the atmosphere is always negative, but longwave cooling can be strongly reduced with the presence of optically thick high cloud.

Incoming solar radiation is the main source of shortwave radiation into the atmosphere (surface albedo is only 0.07 in our simulations). Water vapor is an excellent absorber of shortwave radiation, so the column humidity will have a major effect on the shortwave heating rates. Clouds are also good absorbers of shortwave radiation and act to increase the amount of diffuse radiation, allowing more radiation to be absorbed by cloud and water vapor. However, they are also good reflectors, resulting in clouds having either a positive or negative influence on atmospheric shortwave heating (Wing & Cronin, 2016).

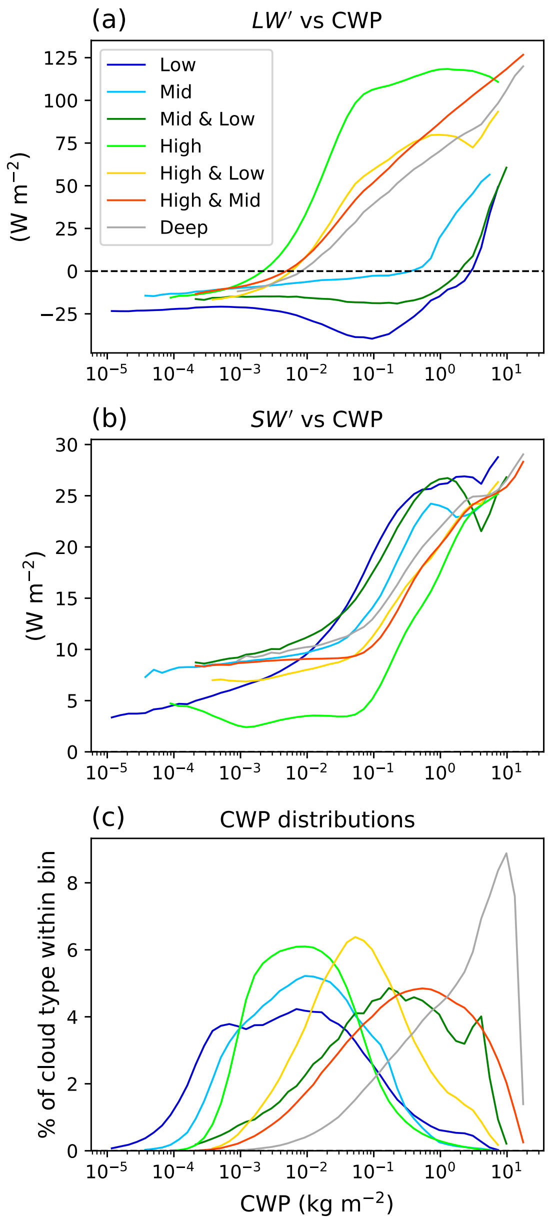

Figure 7. (a) Longwave and (b) shortwave radiative heating anomalies versus condensed water path for each cloud type, and (c) distributions of condensed water path for each cloud type. Data from the *LARGE*, 300 K sea surface temperature simulation during the Mature phase. Fifty bins are spaced logarithmically throughout the condensed water path range. The percentage shown in panel (c) is the percentage of each cloud type within a given bin.

From Figures 6a and 6c, we see a strong connection between cloud and longwave heating anomalies. As previously noted, there is a distinct lack of low cloud in our simulations, so the vast majority of cloud in this figure are high-topped clouds. These high-topped cloud regions have an average longwave heating anomaly of 47 W m^{-2}, with the thicker clouds tending to have higher anomalies. The remaining cloud type regions have an average longwave anomaly of −16 W m^{-2}, and the clear regions have an average of −11 W m^{-2}. The shortwave heating rates are very strongly correlated with $\hat{h}'$. With changes in $\hat{h}$ stemming from changes in water vapor, shortwave heating rates depend mostly on the amount of water vapor in the column, and 99% of the shortwave heating anomalies fall in the range of −15–28 W m^{-2}. Note that radiative fluxes are output as hourly averaged variables whereas FMSE and 3D data (including cloud type classification) are instantaneous snapshots.

We wish to study how the radiative feedbacks of each cloud category contribute to the var($\hat{h}_n$) tendency of the entire domain. Since both radiative anomalies and FMSE anomalies are calculated at each grid point, the instantaneous values of the radiative terms in Equation 4 can also be calculated at each point across the domain. Then, by knowing the cloud type at each grid point, the contributions of each category to the domain-mean radiative terms can be found.

Note that this approach does not describe the cloud-only effect, and since the anomalies of FMSE and radiation also depend on the domain-mean, var($\hat{h}_n$) is not purely a local metric. We only consider the column-integrated cloud-radiative feedbacks here, although indirect radiative interactions with cloud are shown to be important via the generation of circulations (Holloway & Woolnough, 2016; Muller & Bony, 2015). Nevertheless, we find the approach to be a useful way to compare the relative importance of each cloud type's direct radiative contribution to self-aggregation across a range of SSTs.

To begin to quantify the longwave and shortwave heating effects of clouds, the mean radiative anomalies of each cloud type for a given CWP are shown in Figures 7a and 7b. The radiative heating in both the longwave and shortwave varies strongly with CWP. The cloud type is also a very important factor in the radiative anomalies, particularly in the longwave. For a given CWP, High clouds have the largest column longwave heating rates since they have cold cloud tops, resulting in low OLR. This effect, combined with relatively little emission to the surface, leads to strongly positive longwave heating anomalies. Low clouds have warm tops and warm bases, so they effectively emit longwave radiation to space as well as to the surface, cooling the column faster than Clear regions. While Deep clouds emit weakly to space, their low, warm bases strongly emit toward the surface, placing their longwave heating rates in between High and Low clouds for a given CWP.

In the shortwave, each cloud type's heating rate increases with CWP, although this is largely due to increased shortwave absorption by water vapor within these columns (Section 4.3). There is however some dependence on cloud type due to the high reflectivity of clouds. Columns with Low clouds typically have the highest shortwave heating rates. Their low cloud top height allows lots of shortwave radiation to be absorbed by water vapor. The radiation they reflect may also be absorbed by water vapor above the cloud. High clouds have the lowest shortwave heating rates as they reflect a large amount of solar radiation before it can be absorbed by the water vapor below.

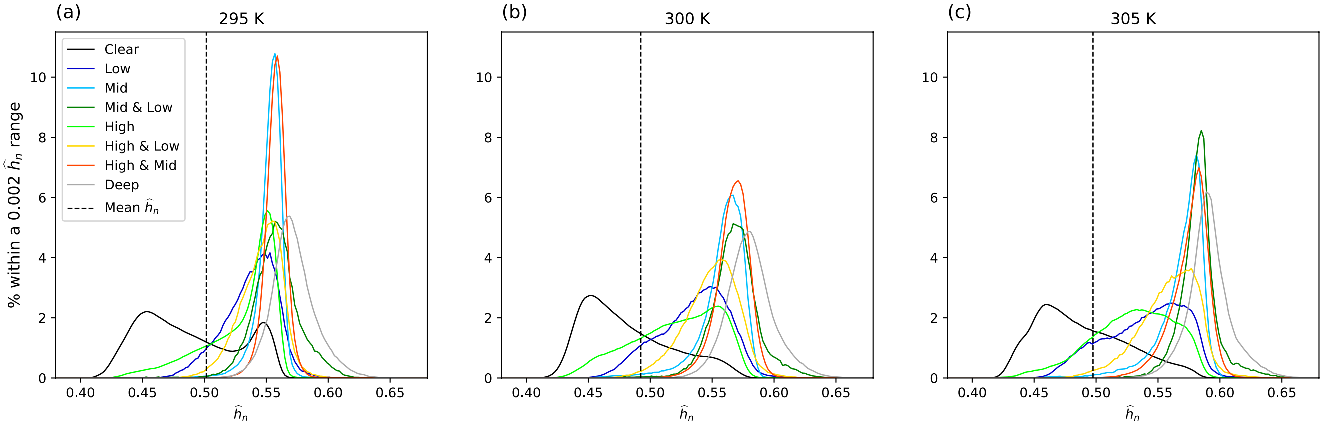

Figure 8. Distributions of $\hat{h}_n$ for each cloud type for all SSTs within the *LARGE* domain during Mature phase. The vertical dashed line indicates the domain-mean $\hat{h}_n$ throughout the Mature phase. Note that each curve is normalized individually.

The distributions of CWP for each cloud type are shown in Figure 7c. These distributions, paired with the dependence of the radiative anomalies on CWP, determine the mean radiative anomalies for each cloud category (domain-averaged heating rates of all categories are shown in Figures 9e–9g). Despite the High clouds having the largest longwave heating rate for a given CWP, their CWP distribution peaks at around 0.01 kg m^{-2}, corresponding to a longwave heating anomaly of roughly 20 W m^{-2}. In contrast, the High & Mid cloud has a peak CWP around 0.5 kg m^{-2} corresponding to a longwave heating anomaly around 70 W m^{-2}. This results in High clouds having only the fourth largest domain-averaged longwave heating rates out of all categories.

Distributions of $\hat{h}_n$ during the Mature phase of the *LARGE* simulations for each cloud category are shown in Figure 8. The vast majority of clouds occur within anomalously high $\hat{h}_n$ regions, with only a few High and Low clouds occurring with negative $\hat{h}'_n$. High clouds have the largest spread of $\hat{h}_n$ out of all the cloud types as they can extend hundreds of kilometers away from the updraft, spanning a wide $\hat{h}_n$ range. Low clouds occur within a broad span of $\hat{h}_n$ as they can form under a wide range of conditions. At higher $\hat{h}'_n$ regions, Low clouds form and may continue to develop into congestus and cumulonimbus, as the environment is favorable for deep convection. At lower $\hat{h}'_n$ regions, descending motion throughout the free troposphere increases stability and reduces humidity, making the atmosphere unfavorable for deep convection, but shallow cumulus may still form atop the well-mixed boundary layer. The majority of the other cloud types are associated with deep convection, which only occurs within high $\hat{h}'_n$ regions, where the environment is favorable for updraft development. Whilst the domain-mean $\hat{h}'_n$ for the Clear regions is slightly negative, there is a very large spread in the distribution of $\hat{h}_n$, with just under half of the Clear regions having positive anomalies.

The domain-mean $\hat{h}_n$, as well as its lower limit, remain very similar with SST. The upper limit increases slightly with SST, as does the mean $\hat{h}_n$ for most cloud types. We do not have a good explanation for this phenomenon.

4.1. Longwave-Cloud Interactions

The contribution of each cloud category to the radiative terms can be calculated by multiplying their mean covariance between the normalized radiative and $\hat{h}$ anomalies by their cloud fraction. Figure 9a shows that it is the Clear, High, High & Mid, and Deep categories that have the largest contribution to the longwave term during the Mature phase (compare open circles representing the Mature phase), with the magnitude of their contributions being highly sensitive to SST. The contributions of the Low, Mid, Mid & Low and High & Low categories have a relatively insignificant contribution. To understand the magnitudes of the contributions of each cloud type to the longwave term, the constituents of the longwave term are shown in the left-hand panels in Figure 9. The figure shows the $LW'_n \times \hat{h}'_n$ covariance, and the fraction of each category.

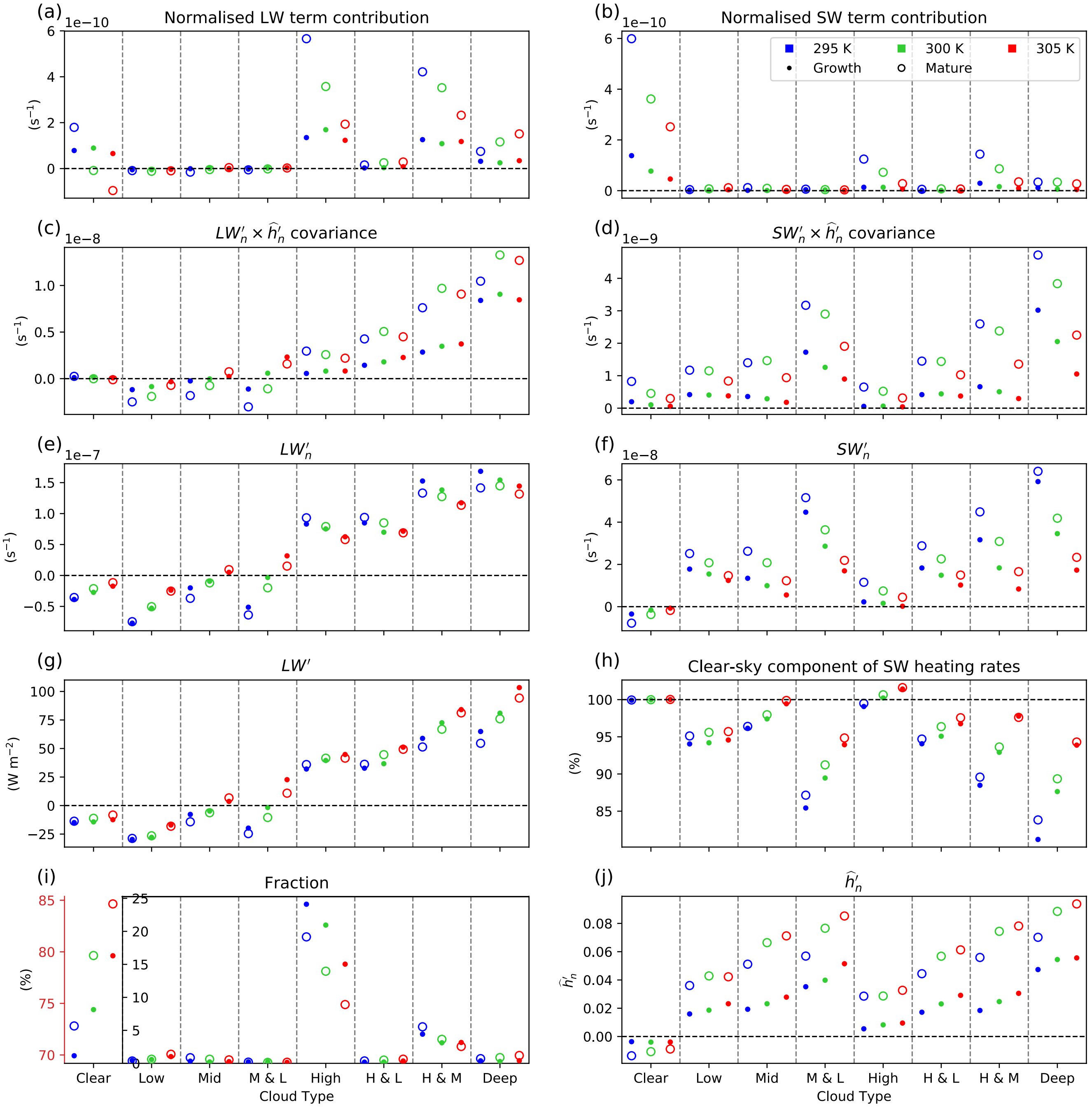

Figure 9. Mean (a) contribution to the longwave term in Equation 4, (b) contribution to the shortwave term, (c) normalized longwave × FMSE covariance, (d) normalized shortwave × FMSE covariance, (e) normalized longwave heating anomaly, (f) normalized shortwave heating anomaly, (g) longwave heating anomaly, (h) clear-sky heating divided by total shortwave heating rate, (i) cloud fraction, and (h) normalized FMSE anomaly for the Growth (dots) and Mature phase (open circles) of the *LARGE* domains. Data points for each category are in order of sea surface temperature increasing to the right. Boxplots showing the spread of the data for the Mature phase are shown in Figure S1.

The mean LW_n' and $\hat{h}_n'$ are also shown, as well as the non-normalized longwave anomaly. Note that the mean LW_n' multiplied by the mean $\hat{h}_n'$ does not equal the mean $LW_n' \times \hat{h}_n'$ covariance, although for most categories they are approximately equal. One notable exception is the $LW_n' \times \hat{h}_n'$ covariance for the Clear regions at 305 K, which is negative, despite having both negative LW_n' and $\hat{h}_n'$. This is discussed in Section 4.2.

Despite their relatively low $LW_n' \times \hat{h}_n'$ covariance, High clouds are one of the main contributors to the longwave term at all SSTs because of their abundance, occurring roughly four times as often as any other cloud type (Figure 9i). The longwave covariances for the High & Mid and Deep clouds are high compared to the other categories, and they are abundant enough to have an impact on the overall longwave term (Figure 9a). Low, Mid, and Low & Mid clouds have a small mean longwave covariance and also a small total fraction, making their contribution to the overall longwave term negligible. Despite having the third-largest longwave covariance, the High & Low cloud type has one of the smallest cloud fractions, making its overall contribution also very small.

There is a significant decrease in the contributions of High and High & Mid clouds to the longwave term as SST increases (Figure 9a). Figure 9c shows that the $LW_n' \times \hat{h}_n'$ covariance remains similar for these cloud types across all SSTs, yet the fraction of these clouds decreases (Figure 9i). This suggests the sensitivity of the High and High & Mid cloud's longwave contribution to aggregation is predominantly due to the sensitivity of their abundance to SST. This decrease in anvil cloud fraction with SST is consistent with the stability iris mechanism described by Bony et al. (2016), who describe the reduction in anvil cloud as a consequence of increased anvil stability and decreased convective outflow with increasing SST. This decrease in high clouds is consistent with ~70% of the other RCEMIP models (Wing et al., 2020).

The net longwave heating rate for all cloud types is negative, and gets more negative with increasing SST (not shown). This SST sensitivity is primarily because the downwelling longwave radiation into the surface increases with SST faster than the upwelling longwave radiation. However, the non-normalized longwave heating anomalies tend to become more positive with SST. As noted in Section 3, Wing and Cronin (2016) hypothesize that the longwave cloud feedback would be more negative at lower SSTs because the atmosphere is so optically thin at cooler SSTs that clouds act as effective longwave emitters, making their LW' more negative. Figure 9g is in agreement with this hypothesis, with LW' for each cloud type being more negative at lower SSTs. Once the longwave anomalies are normalized however, we see there is a slight decrease in LW_n' with increasing SST for the significant cloud types as the difference between $\hat{h}_{\max}$ and $\hat{h}_{\min}$ increases. The decrease in LW_n', along with the slight increase in $\hat{h}_n'$ with SST, results in the $LW_n' \times \hat{h}_n'$ covariance for the most abundant cloud types remaining approximately constant with SST.

4.2. Longwave Interactions Within the Clear Regions

Figure 9a shows the contributions of the Clear regions to the longwave term decrease and become negative with increasing SST. The reason for this is not immediately apparent, with the mean $LW_n' \times \hat{h}_n'$ covariance becoming negative, despite both the mean LW_n' and mean $\hat{h}_n'$ remaining negative (which would usually produce a mean positive covariance). This indicates that there must be a significant proportion of the Clear regions with large negative covariance which is able to reduce the overall contribution to the longwave term with increasing SST.

We consider four types of Clear regions at play here whose significance changes with SST. There are the regions with both positive $\hat{h}'$ and LW' (H+L+), regions with both negative $\hat{h}'$ and LW' (H−L−), positive $\hat{h}'$ and negative LW' (H+L−) and finally, negative $\hat{h}'$ and positive LW' (H−L+). The Clear covariance quadrant map in Figure 6e shows that H+L+ regions are rare and are found in the highest $\hat{h}'$ areas, with a portion of these regions perhaps occurring as an artifact of the condensed water content used to define clouds. A lot of these H+L+ columns may indeed have enough high-altitude condensed water to produce a positive longwave heating anomaly. H+L− regions are typically found surrounding the cloud clusters, with H−L− occupying the majority of the dry regions. H−L+ occur only within the very driest areas. The H+L+ and H−L− regions both have a positive $LW' \times \hat{h}'$ covariance whereas the H−L+ and H+L− regions have a negative covariance. By calculating the domain fraction of these regions, as well as their mean LW_n' and $\hat{h}_n'$ and their mean $LW_n' \times \hat{h}_n'$ covariance, we can see how their influences on the longwave term changes with SST. These calculations are shown in Figure 10 for both the Growth phase and Mature phase of aggregation. The Growth phase is discussed in Section 5.

There is a shift in dominance from the positive covariance regions to the negative covariance regions as the SST increases. For all SSTs, the H+L+ regions only occupy around 1% of the domain, making their overall

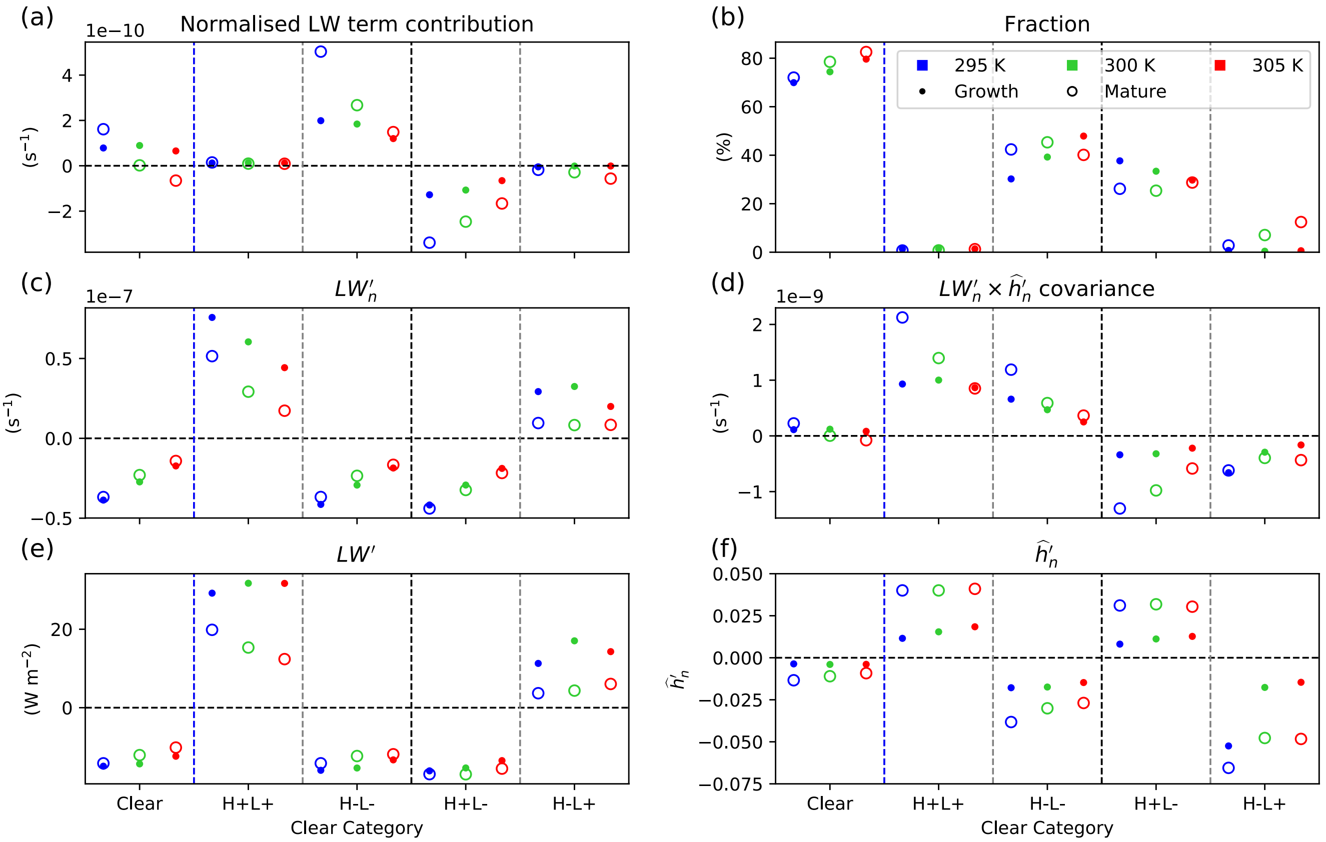

Figure 10. Mean (a) contribution to the normalized longwave term, (b) domain fraction, (c) normalized longwave heating anomaly, (d) mean normalized longwave × FMSE covariance, (e) longwave heating anomaly, and (f) normalized FMSE anomaly of each Clear category for the Growth (dots) and Mature phase (open circles). Boxplots showing the spread of the data for the Mature phase are shown in Figure S2.

contribution to the longwave term negligible. At 295 K, there are two significant Clear regimes; H−L−, occupying 44% of the domain and H+L−, occupying 25%. They have similar but opposite $LW_n' \times \hat{h}_n'$ covariances, so the Clear region's contribution to the longwave term is dominated by the H−L− regions based on their abundance. This results in a positive contribution of the Clear regions to the longwave term.

As SST increases, the LW' of the Clear regions as a whole becomes significantly less negative (Figure 10e). This is mainly due to the approximate halving in the abundance of high-topped clouds, which have strong positive longwave heating anomalies. This then reduces the domain-mean longwave heating rate, making the longwave anomaly of the Clear regions less negative. If we calculate LW' for each category using the absolute longwave heating rates of the cloud types at 295 K and use the cloud type fractions of the 305 K simulations, we find the LW' of the clear regions reduce by ~51%. After normalizing the longwave anomalies, the SST sensitivity is even more notable (Figure 10c). The contribution of the H−L− regions falls rapidly as the $LW_n' \times \hat{h}_n'$ covariance decreases. At the same time, the H−L+ regions (with negative covariance) become far more abundant, also helping to decrease the Clear region's contribution to the longwave term. This feature was also noted by Wing and Emanuel (2014) and Emanuel et al. (2014), who explain that extremely dry columns with little low-level moisture are unable to effectively emit radiation, resulting in anomalous warming.

The magnitude of $\hat{h}'$ is largest for the two regimes with positive LW' (L+, Figure 10f). This is because the relationship between $\hat{h}$ and longwave heating within the Clear regions is not linear; the strongest longwave cooling occurs roughly where $\hat{h}'$ is zero for all SSTs. The effective upward emission level is defined as the altitude at which the temperature is such that σT^4 is equal to the OLR, where σ is the Stefan-Boltzmann constant. Similarly, the effective downward emission level is the altitude at which the temperature is such that σT^4 is equal to the downwelling longwave radiation at the surface. For anomalously moist regions, high humidity in the boundary layer makes the effective downwelling level of emission close to the surface. Therefore, an increase in moisture does little to increase the downwelling longwave radiation. In these regions, an increase in moisture has more of an effect in raising the upwelling level of emission to a cooler level, decreasing OLR, reducing longwave cooling. For anomalously dry regions, the troposphere is very transparent to longwave radiation, so the upwelling level of emission is low (enhanced OLR) and the downwelling level of emission is high (reduced downwelling radiation). In these regions, the free troposphere is very dry, so humidity variations are mainly affected by changes in boundary layer humidity. An increase in humidity in these dry regions has more of an effect in lowering the downwelling level of emission than raising the upwelling level of emission. Therefore, increasing humidity leads to a lowering of the downwelling emission level, increasing downwelling longwave radiation, enhancing longwave cooling. Upwelling and downwelling longwave fluxes are shown as a function of $\hat{h}_n'$ in Figure S3. Specific humidity profiles and effective emission levels as a function of $\hat{h}_n'$ for each SST are shown in Figure S4.

With the mean longwave heating rates skewed more toward the Clear longwave heating rates with increasing SST, there is a greater quantity of Clear regions with positive LW'. This can be seen in the bottom panel of Figure S3, noting the tails of the $\hat{h}_n'$ distributions extend more into the regions with positive longwave heating anomalies as SST increases. This has the effect of lowering the $LW_n' \times \hat{h}_n'$ covariance of the H−L− regions, increasing the contribution of H−L+ regions to the longwave feedback term, and making the total Clear regions' contribution to the longwave term negative at high SSTs.

4.3. Shortwave Interactions

Figure 9b shows that shortwave feedbacks in the Clear regions contribute the most to the shortwave term once the domain is aggregated. However, this is an artifact of the large fraction of the Clear regions. It can be seen from Figures 6b and 6d that there is a very strong relationship between both FMSE and shortwave anomalies. This is because variations of FMSE are dominated by changes in water vapor, which is an excellent absorber of shortwave radiation. This results in the shortwave-FMSE covariance being positive at almost every location (e.g., Arnold & Putman, 2018).

A large portion of the cloud contribution to the shortwave term is due to the amount of water vapor in the column. The contribution of water vapor to the column shortwave heating rate can be quantified by calculating the clear-sky heating rates and dividing by the total heating rates for each category as shown in Figure 9h. The Clear regions have the second-lowest $SW_n' \times \hat{h}_n'$ covariance behind High clouds, yet they contribute the most to the shortwave term due to the abundance of Clear regions. The total shortwave heating rates can almost entirely be explained by the column water vapor path (WVP), particularly at higher temperatures where the quantity of water vapor is higher, making the condensed water content less significant at higher temperatures. The clear-sky component of the total shortwave heating rate is lowest for clouds with the highest CWP since there is a higher fraction of the heating rate due to condensed water. The clear-sky heating rate is sometimes higher than the all-sky heating rate for the high clouds since the cloud reflects the radiation that would otherwise have been absorbed by the low-level water vapor.

The contribution of the shortwave term to aggregation is highly sensitive to SST, becoming less important as SST increases. This is because the range of SW_n' decreases with increasing SST, whereas the range of $\hat{h}_n$ remains similar. This results in the domain-mean normalized shortwave-FMSE covariance, and therefore, the shortwave term, decreasing with SST (analysis not shown). The range of column WVP across the domain increases exponentially with SST, whereas the relationship between column shortwave heating with WVP is logarithmic (Vaquero-Martínez et al., 2018). This results in the range of shortwave heating across the domain being approximately linear. Once the shortwave heating anomalies are divided by $\hat{h}_{max} - \hat{h}_{min}$, SW_n' decreases with increasing SST.

5. Cloud Type Contributions Throughout the Aggregation Process

So far, we have only discussed the radiative interactions within the already-aggregated *LARGE* domains. In this section, we look at the key radiative-convective interactions responsible for the development of aggregation in the Growth phase, studying how these interactions depend on SST, and how they are sensitive to aggregation.

Interactions between $\hat{h}$ and longwave radiation are the main drivers of aggregation at early times (Figure 5d). The longwave term is insensitive to SST during the Growth phase, whereas an SST sensitivity develops once the aggregation is Mature, with the mean longwave term decreasing with SST. Throughout the aggregation process, the magnitude of each cloud type's contribution to both radiative terms tends to increase. This is because the magnitude of $\hat{h}'$ increases, and thus the positive radiative feedbacks increase.

During the Growth phase, the contributions of the different cloud types to the longwave term remain similar with SST, with longwave interactions with high-topped clouds and Clear regions driving aggregation. Perhaps coincidentally, SST trends in the domain fractions of these cloud types are balanced by opposite trends in the $LW_n' \times \hat{h}_n'$ covariance resulting in their contributions to the longwave term being similar.

The development of the negative SST-dependence of the longwave term during the Mature phase can be largely attributed to the amount the high-topped cloud fraction reduces from the Growth phase to the Mature phase, which is greater in relative terms for higher SSTs. The SST trend of the $LW_n' \times \hat{h}_n'$ covariance of High clouds also becomes more negative during the Mature phase. Figure 9g shows that the LW' remains approximately constant with aggregation for all categories, so High clouds' increasingly negative $LW_n' \times \hat{h}_n'$ covariance with SST during the Mature phase has to do with how $\hat{h}_n'$ for High clouds changes with aggregation. The coverage of anvil cloud decreases with SST because of the stability iris mechanism described by (Bony et al., 2016). This allows anvil clouds to extend further away from the updrafts for cooler SSTs, allowing anvil clouds to occur in lower FMSE regions. This effect is enhanced with disaggregated convection where the horizontal scale of the moist regions is small. For aggregated convection, the moist regions are much larger in size, so even anvils that extend far beyond the updraft will remain in anomalously moist environments, enhancing the longwave-FMSE feedback. Therefore, the $\hat{h}_n'$ of High clouds increases less with aggregation at higher SSTs. This, combined with the decrease in high-topped cloud fraction with SST, decreases the cloud contribution to the longwave feedback during the Mature phase as SST increases.

The longwave feedback in the Clear regions is positive and insensitive to SST during the Growth phase. The H−L− and H+L− categories are the only Clear categories that have a significant impact during the Growth phase with the H−L− having the largest contribution to the longwave term (Figure 10a). During the Growth phase, the contribution of the H−L− category remains similar since the increase in its fraction with SST is perhaps coincidentally balanced by the decrease in $LW_n' \times \hat{h}_n'$ covariance. As the convection becomes more aggregated, the fraction of the H−L− regions becomes more constant with SST. The $LW_n' \times \hat{h}_n'$ covariance also becomes increasingly negative with SST because $\hat{h}_n'$ becomes less anomalously negative. These factors result in the longwave feedback of the Clear regions developing the negative SST dependence once the convection aggregates.

Wing and Cronin (2016) find the clear-sky longwave feedback increases with SST particularly during the Growth phase, which is consistent with the simple two-layer model outlined in Emanuel et al. (2014) that suggests the clear-sky longwave feedback becomes more positive with SST. This is because at low SSTs, the tropospheric longwave opacity is low, so an increase in humidity results in an increase in atmospheric longwave cooling (negative feedback). At high SSTs, the tropospheric longwave opacity is higher due to increased water vapor. Here, an increase in humidity results in a decrease in longwave cooling (positive feedback). We find the Clear regions' longwave contribution to the domain-mean longwave feedback is similar with SST during the Growth phase, then decreases with SST during the Mature phase. This effect is not a disagreement with those studies, as this study does not consider the clear-sky radiative fluxes separately. Instead, we only use the total radiative fluxes and we break down the domain-mean longwave feedback into contributions from Clear and cloudy regions. Our study finds the longwave contribution of the Clear regions decreases with SST because their longwave cooling becomes less anomalous with SST due to the reduction of high-topped clouds.

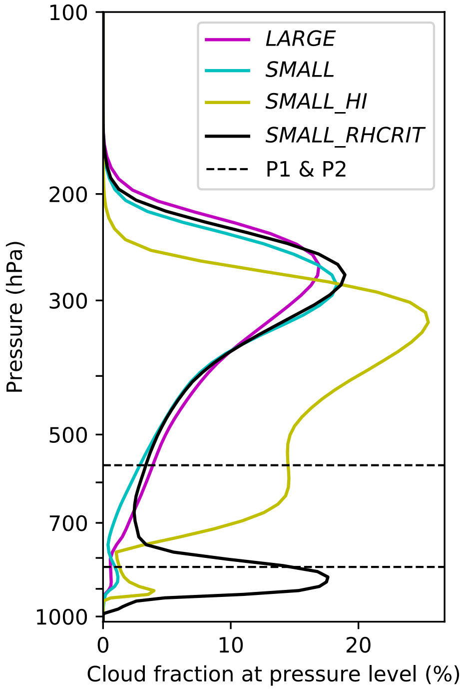

Figure 11. Temporally averaged cloud fraction profiles after the spin-up period and while var($\hat{h}_n$) < 4×10^{-4} for each domain setup at 295 K. Horizontal dashed lines represent the low and high cloud thresholds (P1 and P2).

The shortwave interactions become less significant for driving aggregation as SST increases. The clear-sky shortwave contribution is inversely proportional to the difference between $\hat{h}_{\max}$ and $\hat{h}_{\min}$, and the difference in shortwave absorption between cloudy and clear regions decreases with SST as the atmosphere contains more water vapor. This results in the shortwave interactions being approximately 2.5 times more important in driving aggregation at 295 K compared to 305 K (Figures 5d and 9b).

The shortwave anomalies increase in magnitude as aggregation increases, since the cloudy regions become more humid and the clear regions become drier, amplifying the shortwave heating anomalies. Because of this, the shortwave feedback is more effective in maintaining aggregation than driving it. However, at very early times, particularly for cooler SSTs, the shortwave absorption by clouds can have a significant impact on increasing aggregation. This can be seen in Figure 9h, with the clear-sky component contributing more to shortwave heating during the Mature phase, and also in the time series of the clear-sky component of the shortwave term (using clear-sky radiative transfer calculations) shown in Figure S5. At very early times, there is little variation in horizontal distribution of water vapor, so the shortwave absorption by clouds has a significant impact on the mean $SW_n' \times \hat{h}_n'$ covariance. At these times, the shortwave absorption by clouds accounts for between 30% and 50% of the shortwave term, with clouds having a larger impact at colder SSTs due to the decrease in tropospheric water vapor. This SST dependence is consistent with Wing and Cronin (2016). As soon as dry and moist patches begin to develop, the horizontal variations in the shortwave absorption of water vapor dominate the shortwave term, accounting for 87%–96% of the shortwave term as SST increases once the domains are aggregated.

6. Comparison of Convection Within High-Resolution Simulations

In the previous sections, only radiative interactions within *LARGE* domain simulations have been analyzed. In addition to these, we have also simulated the three-SST RCEMIP cases in three other model configurations on smaller (100 km × 100 km) domains to investigate how radiative interactions with clouds and moisture may be affected by horizontal grid spacing and the treatment of subgrid condensation. Our *SMALL* and *SMALL_RHCRIT* simulations have a grid spacing of 1 km, while the *SMALL_HI* simulations have a grid spacing of 0.1 km. While the *SMALL* and *SMALL_HI* both have a uniform RHcrit parameter of 99%, the *SMALL_RHCRIT* simulations have RHcrit decreasing from 96% near the surface to 80% at 900 m and above.

With the length scale of the aggregated features in the *LARGE* domain being many times larger than the dimensions of our smaller simulations, we are not able to quantify how these changes in resolution and RHcrit explicitly affect aggregation. However, we are able to see how the radiative properties of the clouds are affected. We can then infer how these changes in the radiative properties of cloud may impact aggregation in larger-scale simulations.

Convection displays some degree of aggregation in all of our simulations except for the *SMALL_HI* 295 K case. On average, the large domain simulations reach a maximum var($\hat{h}_n$) of 2.5×10^{-3}, the *SMALL* and *SMALL_RHCRIT* simulations reach 1.2×10^{-3}, and the *SMALL_HI* simulations reach an average of 0.21×10^{-3}. The 295 K *SMALL_HI* simulation is the only simulation that displays no aggregation. Time series of var($\hat{h}_n$) for each domain and SST are shown in Figure S6. To compare radiative interactions with clouds across our domains disregarding the influence of strong aggregation, we compare times at which var($\hat{h}_n$) is less than 4×10^{-4}. We also neglect the first 2 days of the *LARGE*, *SMALL*, and *SMALL_RHCRIT*, and the first 5 days of the *SMALL_HI* simulations, to ignore the spin-up phase of the simulations

Profiles of cloud fraction reveal that both grid spacing and RHcrit strongly influence the vertical structure of clouds across the domain (Figure 11). This figure shows only the 295 K simulations, although similar

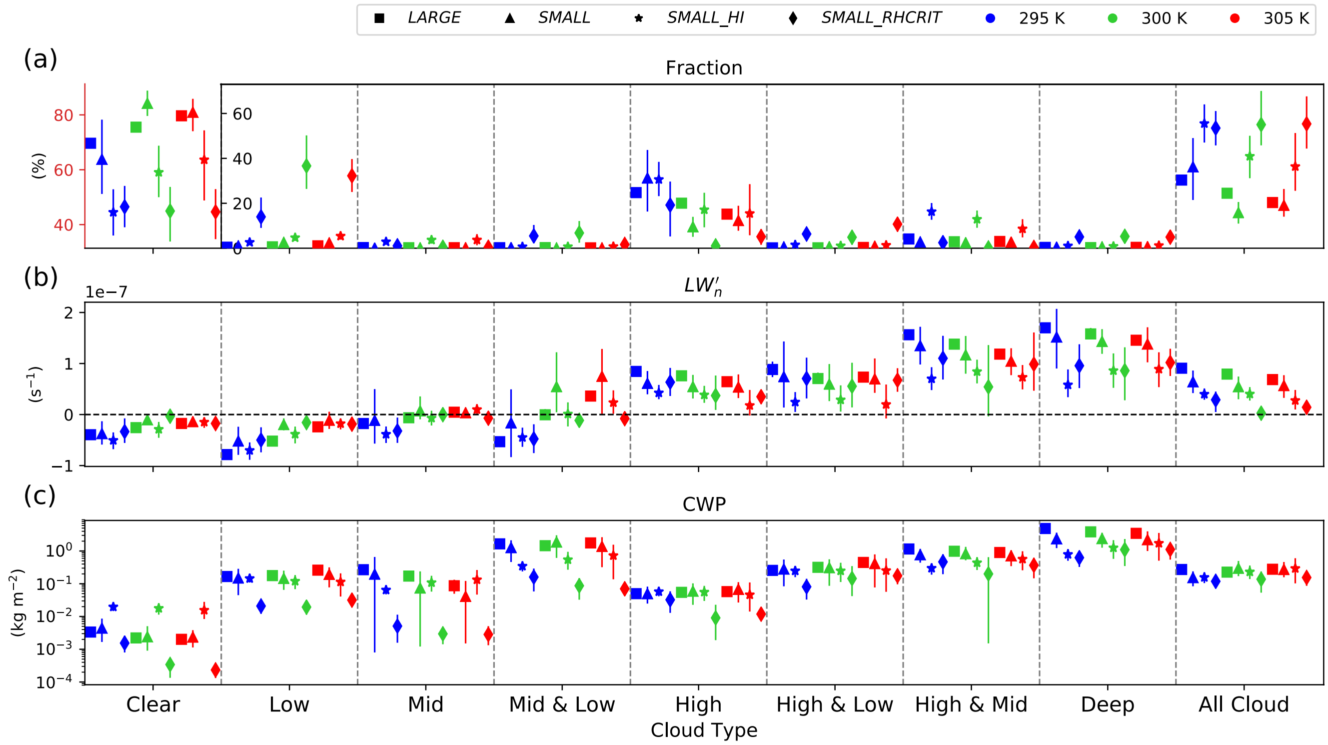

Figure 12. Instantaneous domain-means of (a) domain fraction, (b) normalized longwave heating anomaly, and (c) condensed water path, for each cloud category within all domain setups and SSTs. Data taken after the spin-up period and while var($\hat{h}_n$) < 4×10^{-4} for each domain setup at 300 K. Note that the fraction of the Clear regions (top-left panel) are on a separate axis to the remaining cloud types. Vertical bars represent the range of the 10th to 90th percentile.

changes are seen at the other SSTs. As the grid spacing is reduced, there is a sharp increase in the quantity of low and mid-level cloud, with this increase being most apparent when looking at the *SMALL_HI* simulation. Low-level clouds generally have smaller length scales so cannot be resolved in coarser grid spacings due to the unrealistically high RHcrit value used. Our original RHcrit value becomes more suitable at lower grid spacings, effectively representing these small-scale clouds more realistically. There is also a decrease in the altitude of high-level clouds with decreasing grid spacing.

As the RHcrit is decreased to that used in the Met Office UKV model, the overall cloud amount increases. This comes from an increase of more than an order of magnitude in the low-level cloud and also a significant increase in the mid-level cloud. The upper-level cloud amounts remain largely unchanged. Fractions of the High, and High & Mid cloud types are greatly reduced due to the increase in low and mid-level clouds, in turn increasing the quantities of the High & Low and Deep cloud types.

Longwave interactions with FMSE are the main drivers of aggregation in our models (Section 3, Figure 5). With cloud-longwave heating rates remaining largely insensitive to aggregation, a fair comparison of cloud-longwave interactions across our domains can be made. We do not compare the FMSE anomalies of the cloud types as the degrees of aggregation, and hence FMSE anomalies of different cloud types, are very different across the domains, despite neglecting the mature phase of aggregation. We also do not compare the shortwave heating anomalies for the same reason. With shortwave heating rates being mostly dependent on the column water vapor, the changes in shortwave heating rates due to the resolution dependence of cloud structures would be overshadowed by the effects of different degrees of aggregation.

Comparisons of cloud type fraction, normalized longwave, and CWP for each cloud category, SST, and domain configuration are shown in Figure 12. From this, the resolution dependence of the longwave term for self-aggregation may be inferred. There is a significant decrease in the longwave heating rates of high-topped clouds with both decreasing grid spacing and decreasing RHcrit. This is mainly due to an increase in OLR rather than an increase in the downwelling longwave radiation which remains approximately constant for these categories with grid spacing (not shown). This increase in OLR may be mostly explained by the change in cloud top height as well as the decrease of CWP. There is an associated increase in cloud top temperature with decreasing altitude, which increases OLR. One plausible explanation for the reduced cloud top height is that increased updraft mixing at higher resolutions decreases updraft buoyancy and thus reduces the maximum altitude of the plume (this analysis is outside the scope of our paper). The CWP decreases for the majority of cloud types as the critical condensation humidity is reached more widely, that is, by decreasing RHcrit or decreasing the grid spacing. Since water vapor is more readily condensed, the clouds that do form are more widespread and less concentrated. A decreasing CWP of these high-topped clouds decreases their opacity to longwave radiation, decreasing the effective level of emission. This also increases OLR, helping to lower their longwave heating rates.

The longwave heating rates of the remaining cloud categories without high-level cloud remain similar with grid spacing and RHcrit. As shown in Figure 7a, the longwave heating rates of these cloud types are less dependent on CWP in the *LARGE* simulations. The combined fractions of the lower longwave heating rate categories (the combined sum of the Clear, Low, Mid, and Mid & Low categories) remain similar with resolution and RHcrit, and remain far more abundant than the high-topped cloud categories with relatively high longwave heating rate categories. This reduces the spread of longwave heating rates across the domain, decreasing the magnitude of the longwave anomalies for the majority of categories. This may decrease the $LW_n^{'} \times \hat{h}_n^{'}$ covariance in moist regions and may significantly reduce the longwave term. An increase in Low and Mid & Low cloud may also significantly reduce the longwave term since they have strong negative heating rates and are mainly found in positive FMSE anomaly regions so have a negative $LW_n^{'} \times \hat{h}_n^{'}$ covariance on average.

Figure 11 shows that as grid spacing is reduced, there is a large increase in cloud fraction in the mid-troposphere. This results in the fraction of the High category decreasing, and the High & Mid and Deep category fractions increasing. These categories typically have higher $LW_n^{'}$ than High clouds. However, the mean $LW_n^{'}$ of all clouds in the domain is reduced as grid spacing is reduced. With clouds tending to occur in high-FMSE regions, the domain-mean longwave term would likely be reduced. We find a similar result in the reduced RHcrit simulations. With an increase in the low-level cloud, the domain fractions of the High and High & Mid categories decrease, whereas the fraction of Deep clouds increases. Again, Deep clouds tend to have very high $LW_n^{'}$, however the mean $LW_n^{'}$ of all the clouds is again reduced, and is mainly a result of the increased Low cloud fraction with negative $LW_n^{'}$.

In our *LARGE* simulations, the contributions of longwave interactions with FMSE to aggregation decrease with SST as anvil cloud fraction reduces. These cloud-radiation trends with SST are largely consistent with those in the simulations with different grid spacing (*SMALL* and *SMALL-HI*). The total high-topped cloud fraction decreases with SST by a similar amount, as does the decrease in $LW_n^{'}$ for these clouds, meaning trends in the radiative terms to aggregation with SST would likely be similar. For the *SMALL_RHCRIT* simulations however, with Low cloud approximately doubling from 295 to 305 K, the magnitude of the longwave term would decrease faster with SST than our original higher-RHcrit simulations. In the *LARGE* simulations, we also find that Clear regions have a significant positive contribution to aggregation at cooler SSTs, with this contribution decreasing with SST and becoming negative. The longwave heating rates of high-topped clouds are more negative in the reduced RHcrit simulations, in turn increasing the domain-mean longwave cooling. This makes the longwave heating anomalies of the Clear regions less negative, which would further lower the Clear contributions to the longwave term. This remains a consistent trend across all of our simulations.

These results can be used to infer how aggregation may be affected in large domains with smaller grid spacings and at the lower RHcrit. Reductions in both grid spacing and RHcrit are associated with a decrease in the anomalous longwave heating of high-topped clouds and an increase in Low cloud fraction. These effects increase the mean radiative cooling of the entire domain, making the clear regions' longwave cooling less anomalous. With reduced anomalous longwave heating in high-FMSE regions and reduced anomalous cooling in low-FMSE regions, the $LW_n^{'} \times \hat{h}_n^{'}$ covariance would be reduced on average across the domain, slowing the rate of aggregation.

7. Conclusions

In this study, we quantify the dominant direct radiative interactions that drive and maintain aggregation within large channel domain simulations of RCE of the Met Office Unified Model version 11.0 (submitted to RCEMIP as "UMKOi-vn11.0-RA1-T"; Wing et al., 2018). We have assessed the sensitivity of these interactions to SST by comparing simulations with fixed SSTs of 295, 300, and 305K using the normalized vertically integrated FMSE ($\hat{h}_n$) variance budget as our framework for studying self-aggregation. We define the "Growth" and "Mature" phases of aggregation using specific ranges of normalized FMSE to ensure a fair comparison of convection across our simulations during these periods. We particularly focus on the role of cloud-radiative interactions, assigning one of eight different cloud types to each grid column based on the heights at which cloud occurs. We also investigate how the key radiative interactions are affected by both grid spacing and the critical condensation relative humidity parameter (RHcrit) using smaller (100 km × 100 km) domains.

$\hat{h}$ is normalized between an upper and lower limit that are functions of SST, giving values of $\hat{h}_n$ between 0 and 1. Variations in $\hat{h}_n$ are dominated by variations in moisture for all of our SSTs. The difference between the upper and lower limits of $\hat{h}$ is proportional to the magnitude of the FMSE anomalies, making $\hat{h}_n$ approximately SST-independent.

The instantaneous horizontal variance of normalized vertically integrated FMSE, var($\hat{h}_n$), is a consistent aggregation metric across all SSTs, with values below 10^{-4} corresponding to randomly scattered convection, and values greater than 10^{-3} corresponding to highly aggregated convection. The var($\hat{h}_n$) budget equation (Equation 4) states how the rate of change of var($\hat{h}_n$), and hence the rate of change of aggregation, is driven by feedbacks between anomalies in $\hat{h}_n$ and anomalies in normalized column-integrated longwave heating, shortwave heating, surface fluxes, and advection of $\hat{h}_n$. This study focuses on the two radiative feedback terms of this equation (longwave and shortwave), which show that regions with a positive covariance between the normalized radiative anomalies (LW_n' and SW_n') and $\hat{h}_n'$ help to increase aggregation.

During the Growth phase of aggregation, the longwave radiative term in Equation 4 is the main driver in increasing the horizontal variance of $\hat{h}_n$, hence increasing aggregation. The shortwave term is positive, though highly sensitive to SST, contributing 2.5 times more to increasing var($\hat{h}_n$) at 295K than 305K. The surface flux feedback is almost always negative in our simulations and becomes increasingly positive with increasing SST, resulting in the sum of the diabatic terms remaining similar during the Growth phase of aggregation. Despite the sum of the diabatic terms being similar across SSTs, the rate of aggregation increases with SST. This is because the (usually negative) advection feedback becomes increasingly positive with SST during the early stages of aggregation. This allows anomalies in $\hat{h}_n$ to amplify more readily at higher SSTs.

During the Mature stage, both radiative terms are key maintainers of aggregation, with the shortwave term being approximately three-quarters of the magnitude of the longwave term. The longwave term's contribution to the maintenance of var($\hat{h}_n$) decreases with SST during the maintenance phase, as does the shortwave term's contribution. The decrease in these terms is then balanced by an increase in the (negative) surface flux and advection terms.

High-topped clouds produce the largest positive column-integrated longwave heating anomalies, whereas low-level clouds produce negative anomalies. The mean $\hat{h}_n'$ for each cloud type is positive, therefore clouds with a positive radiative anomaly have a positive radiative-FMSE feedback and vice versa. Longwave interactions with high-topped clouds are the main drivers of aggregation because they have a high $LW_n' \times \hat{h}_n'$ covariance and they are the most abundant types of cloud. The contributions from these cloud types remain similar with SST during the Growth phase, however, their contributions to the maintenance of aggregation decrease with SST as cloud fraction decreases.

Longwave interactions within the clear regions can have a large impact on the total longwave term, although their contributions to the longwave term are highly sensitive to SST and aggregation. The longwave contribution of the clear regions is large and positive during the early stages of aggregation and decreases with aggregation and SST, becoming strongly negative during the fully aggregated stage of the high-SST simulation. We show that once the convection is aggregated, the typically negative longwave heating anomalies in the clear regions become less negative with SST as a result of the domain-mean longwave heating becoming increasingly negative. This is due to the reduction of high-topped clouds which have a strong anomalous longwave heating effect, increasing the domain-mean radiative cooling, resulting in the mean longwave heating anomaly of the clear regions becoming roughly 50% less negative. The mean covariance between the longwave heating and FMSE anomalies becomes negative, meaning the clear regions have a negative contribution to aggregation at high SSTs.

The domain-mean shortwave term is similar in magnitude to the longwave term during the Mature phase because the $SW_n' \times \hat{h}_n'$ covariance is positive at almost all times and locations. The mean shortwave-FMSE feedback is heavily dependent on the horizontal spread of water vapor and therefore the state of aggregation, being less important in driving aggregation than maintaining it. The contribution of clouds to the shortwave term also depends on the level of aggregation. At very early times, the additional shortwave absorption of condensed water results in clouds contributing to around 50% of the shortwave term at 295K and 30% at 305K SST. As soon as distinct moist and dry patches begin to develop, the differential absorption of shortwave radiation by water vapor rapidly increases the clear-sky component of the shortwave term to 87%–96% of the total shortwave term (from 295 to 305K).

Model grid spacing affects the radiative properties of clouds in a number of ways. We find that decreasing grid spacing reduces the mean CWP of clouds, decreases the cloud top height of high clouds, and produces more low and mid-level cloud. The overall effect of these changes to the cloud properties is a reduced mean longwave heating anomaly of high-FMSE cloudy regions. This would decrease the domain-mean covariance between longwave heating and FMSE anomalies, slowing the rate of aggregation for hypothetical high-resolution large-domain simulations. Sensitivities with SST that we find in the large domain remain similar with grid spacing, meaning the magnitude of the decrease in the longwave term with SST would likely remain similar with reduced grid spacing in larger simulations.

The RHcrit parameter used in our simulations is unrealistically high for the grid spacings used, resulting in unrealistic cloud distributions. When lowering the RHcrit to that used in the Met Office UKV model, we find significant changes in the distribution, structure, and radiative properties of cloud. The combined effects of using the decreased RHcrit would likely reduce the direct longwave contributions to aggregation. First, the CWP of high clouds reduces as RHcrit is decreased although their domain-fraction remains similar. The reduced CWP decreases their longwave heating anomalies and would significantly reduce their contribution to the longwave term. Second, there is a large increase in the fraction of low cloud, which would likely further reduce the longwave term due to low cloud's typically negative $LW_n' \times \hat{h}_n'$ covariance. However, with the increase in low cloud, the radiatively driven low-cloud circulations described by Muller and Bony (2015) could become more common, increasing the upgradient transport of FMSE. It is not clear whether this indirect low cloud effect would overcompensate, increasing the rate of aggregation.

The vertical distribution of clouds in our models makes these simulations outliers compared to other models submitted to RCEMIP (Wing et al., 2020). Our large-channel simulations have the lowest low-level cloud fraction and one of the highest high-cloud fractions out of the other submitted cloud-resolving models. With high-topped clouds generally having strongly positive $LW_n' \times \hat{h}_n'$ covariances, and low clouds having negative, the domain-mean longwave-FMSE feedbacks may be unusually high. Previous literature has highlighted the importance of upgradient FMSE transport by shallow overturning circulations associated with low clouds (Muller & Bony, 2015). These circulations could be less prevalent in our simulations compared to other RCEMIP simulations, and may result in the advection feedback in our simulations being lower than simulations with a more realistic vertical cloud distribution.

There is much variability in the degrees of aggregation and within numerical models of RCE, which has important consequences for weather and climate (Wing et al., 2020). With radiative interactions between cloud and moisture being the dominant drivers and maintainers of aggregation in our models, understanding how these interactions vary between other RCE models may go some way in explaining the differences in self-aggregation and this is a focus of our ongoing work. By building on the analysis technique of Wing and Emanuel (2014), this paper provides a framework by which a comparison of cloud-radiative interactions and their contributions to self-aggregation between models and SSTs can be achieved. This technique is suitable for all models with a fixed SST. Its use for model/reanalysis studies with a varying SST would require the normalization of $\hat{h}$ to vary in space and time.

Appendix A: Normalized FMSE Variance Budget Equation Derivation

Starting with the equation of normalized FMSE:

$$\hat{h}_n = \frac{\hat{h} - \hat{h}_{min}}{\hat{h}_{max} - \hat{h}_{min}} \tag{A1}$$

$\hat{h}_n$, can be broken down into its domain-mean state plus the anomaly from the mean:

$$\hat{h}_n = \{\hat{h}_n\} + \hat{h}_n' \tag{A2}$$

where curly brackets denote the domain-mean state. Splitting $\hat{h}_n$ and $\hat{h}$ in Equation A1 into their domain mean and anomaly, we get:

$$\{\hat{h}_n\} + \hat{h}_n' = \frac{\{\hat{h}\} - \hat{h}_{min}}{\hat{h}_{max} - \hat{h}_{min}} + \frac{\hat{h}'}{\hat{h}_{max} - \hat{h}_{min}} \tag{A3}$$

The first term on both sides of the equation is the domain-mean of $\hat{h}_n$ and the second term is the anomaly. By subtracting the domain-mean from this equation, we end up with an expression for the anomaly of $\hat{h}_n$:

$$\hat{h}_n' = \frac{\hat{h}'}{\hat{h}_{max} - \hat{h}_{min}} \tag{A4}$$

Differentiating this with respect to time:

$$\frac{\partial \hat{h}_n'}{\partial t} = \frac{1}{\hat{h}_{max} - \hat{h}_{min}} \frac{\partial \hat{h}'}{\partial t} \tag{A5}$$

Multiplying with $\hat{h}_n'$, using the identity $x \times \partial x / \partial t = 1/2 \times \partial x^2 / \partial t$ on the left-hand side, and substituting Equation A4 for $\hat{h}_n'$ on the right-hand side:

$$\frac{1}{2}\frac{\partial \hat{h}_n'^2}{\partial t} = \frac{\hat{h}'}{(\hat{h}_{max} - \hat{h}_{min})^2} \frac{\partial \hat{h}'}{\partial t} \tag{A6}$$

Taking the anomaly of the expression for the tendency of $\hat{h}$ shown in Equation 3 of Wing and Emanuel (2014):

$$\frac{\partial \hat{h}'}{\partial t} = SEF' + LW' + SW' - \nabla_h . \widehat{\mathbf{u}h} \tag{A7}$$

Substituting this into Equation A6 gives us an expression for the $\hat{h}_n$ tendency budget in terms of $\hat{h}'$:

$$\frac{1}{2}\frac{\partial \hat{h}_n'^2}{\partial t} = \frac{\hat{h}' LW' + \hat{h}' SW' + \hat{h}' SEF' - \hat{h}' \nabla_h . \widehat{\mathbf{u}h}}{(\hat{h}_{max} - \hat{h}_{min})^2} \tag{A8}$$

Or in terms of $\hat{h}_n'$, the equation becomes:

$$\frac{1}{2}\frac{\partial \hat{h}_n'^2}{\partial t} = \hat{h}_n' LW_n' + \hat{h}_n' SW_n' + \hat{h}_n' SEF_n' - \hat{h}_n' \nabla_h . \widehat{\mathbf{u}h_n} \tag{A9}$$

Here, each normalized variable is equal to the original variable in Equation 3 divided by the difference between $\hat{h}_{\mathrm{max}}$ and $\hat{h}_{\mathrm{min}}$.

Data Availability Statement

The authors thank the German Climate Computing Center (DKRZ) for hosting the standardized RCEMIP data for the *LARGE* and *SMALL* simulations, which are publicly available at http://hdl.handle.net/21.14101/d4beee8e-6996-453e-bbd1-ff53b6874c0e. All data used for plotting each figure, as well as the original python scripts are available on Zenodo at https://doi.org/10.5281/zenodo.5211557.

References

Arakawa, A., & Schubert, W. H. (1974). Interaction of a cumulus cloud ensemble with the large-scale environment, Part 1. *Journal of the Atmospheric Sciences*, *34*, 674–701. https://doi.org/10.1175/1520-0469(1974)031<0674:IOACCE>2.0.CO;2

Arnold, N. P., & Putman, W. M. (2018). Nonrotating convective self-aggregation in a limited area AGCM. *Journal of Advances in Modeling Earth Systems*, *10*(4), 1029–1046. https://doi.org/10.1002/2017MS001218

Acknowledgments

This work was supported by the Natural Environment Research Council SCENARIO DTP (NE/L002566/1). The simulations of the UM have been produced by Todd Jones, supported by the Natural Environment Research Council (NERC) under the joint NERC/Met Office ParaCon program's Circle-A project (NE/N013735/1), as well as the ParaCon Phase 2 project: Understanding and Representing Atmospheric Convection across Scales (NE/T003871/1). The simulations have been conducted using Monsoon2, a High Performance Computing facility funded by the Met Office and NERC, the NEXCS High Performance Computing facility funded by NERC and delivered by the Met Office, and JASMIN, the UK collaborative data analysis facility. The authors thank Tobias Becker and Allison Wing for insightful reviews that significantly improved the manuscript. The authors also acknowledge Mike Whitall (UK Met office) and Steve Woolnough (University of Reading) for their valuable insights and suggestions.

Arnold, N. P., & Randall, D. A. (2015). Global-scale convective aggregation: Implications for the Madden-Julian Oscillation. *Journal of Advances in Modeling Earth Systems*, *7*, 1499–1518. https://doi.org/10.1002/2015MS000498

Bao, J., & Sherwood, S. C. (2019). The role of convective self-aggregation in extreme instantaneous versus daily precipitation. *Journal of Advances in Modeling Earth Systems*, *11*(1), 19–33. https://doi.org/10.1029/2018MS001503

Becker, T., Stevens, B., & Hohenegger, C. (2017). Imprint of the convective parameterization and sea-surface temperature on large-scale convective self-aggregation. *Journal of Advances in Modeling Earth Systems*, *9*, 1488–1505. https://doi.org/10.1002/2016MS000865

Becker, T., & Wing, A. A. (2020). Understanding the extreme spread in climate sensitivity within the Radiative-Convective Equilibrium Model Intercomparison Project. *Journal of Advances in Modeling Earth Systems*, *12*, e2020MS002165. https://doi.org/10.1029/2020MS002165

Beucler, T., & Cronin, T. (2019). A budget for the size of convective self-aggregation. *Quarterly Journal of the Royal Meteorological Society*, *145*(720), 947–966. https://doi.org/10.1002/qj.3468

Bony, S., Stevens, B., Coppin, D., Becker, T., Reed, K. A., Voigt, A., & Medeiros, B. (2016). Thermodynamic control of anvil cloud amount. *Proceedings of the National Academy of Sciences of the United States of America*, *113*(32), 8927–8932. https://doi.org/10.1073/pnas.1601472113

Bretherton, C. S., Blossey, P. N., & Khairoutdinov, M. (2005). An energy-balance analysis of deep convective self-aggregation above uniform SST. *Journal of the Atmospheric Sciences*, *62*(12), 4273–4292. https://doi.org/10.1175/JAS3614.1

Bush, M., Allen, T., Bain, C., Boutle, I., Edwards, J., Finnenkoetter, A., et al. (2020). The first Met Office Unified Model-JULES Regional Atmosphere and Land configuration, RAL1. *Geoscientific Model Development*, *13*(4), 1999–2029. https://doi.org/10.5194/gmd-13-1999-2020

Charney, J. G., & Phillips, N. A. (1953). Numerical integration of the quasi-geostrophic equations for barotropic and simple baroclinic flows. *Journal of the Atmospheric Sciences*, *10*(2), 71–99. https://doi.org/10.1175/1520-0469(1953)010<0071:NIOTQG>2.0.CO;2

Coppin, D., & Bony, S. (2015). Physical mechanisms controlling the initiation of convective self-aggregation in a General Circulation Model. *Journal of Advances in Modeling Earth Systems*, *7*, 2060–2078. https://doi.org/10.1002/2015MS000571

Coppin, D., & Bony, S. (2018). On the interplay between convective aggregation, surface temperature gradients, and climate sensitivity. *Journal of Advances in Modeling Earth Systems*, *10*(12), 3123–3138. https://doi.org/10.1029/2018MS001406

Edwards, J. M., & Slingo, A. (1996). Studies with a flexible new radiation code. I: Choosing a configuration for a large-scale model. *Quarterly Journal of the Royal Meteorological Society*, *122*(531), 689–719. https://doi.org/10.1002/qj.49712253107

Emanuel, K., Wing, A. A., & Vincent, E. M. (2014). Radiative-convective instability. *Journal of Advances in Modeling Earth Systems*, *6*, 75–90. https://doi.org/10.1002/2013MS000270

Held, I. M., Helmer, R. S., & Ramaswamy, V. (1993). Radiative-convective equilibrium with explicit two-dimensional moist convection. *Journal of the Atmospheric Sciences*, *50*(23), 3909–3927. https://doi.org/10.1175/1520-0469(1993)050<3909:RCEWET>2.0.CO;2

Hill, P. G., Allan, R. P., Chiu, J. C., Bodas-Salcedo, A., & Knippertz, P. (2018). Quantifying the contribution of different cloud types to the radiation budget in Southern West Africa. *Journal of Climate*, *31*(13), 5273–5291. https://doi.org/10.1175/JCLI-D-17-0586.1

Holloway, C. E., Wing, A. A., Bony, S., Muller, C., Masunaga, H., L'Ecuyer, T. S., & Zuidema, P. (2017). Observing convective aggregation. *Surveys in Geophysics*, *38*(6), 1199–1236. https://doi.org/10.1007/s10712-017-9419-1

Holloway, C. E., & Woolnough, S. J. (2016). The sensitivity of convective aggregation to diabatic processes in idealized radiative-convective equilibrium simulations. *Journal of Advances in Modeling Earth Systems*, *8*, 166–195. https://doi.org/10.1002/2015MS000511

Houze, R. A. (2004). Mesoscale convective systems. *Reviews of Geophysics*, *42*(4), RG4003. https://doi.org/10.1029/2004RG000150

Kiladis, G. N., Wheeler, M. C., Haertel, P. T., Straub, K. H., & Roundy, P. E. (2009). Convectively coupled equatorial waves. *Reviews of Geophysics*, *47*(2), RG2003. https://doi.org/10.1029/2008RG000266

Lock, A. P., Brown, A. R., Bush, M. R., Martin, G. M., & Smith, R. N. B. (2000). A new boundary layer mixing scheme. Part I: Scheme description and single-column model tests. *Monthly Weather Review*, *128*(9), 3187–3199. https://doi.org/10.1175/1520-0493(2000)128<3200:ANBLMS>2.0.CO;2

Madden, R. A., & Julian, P. R. (1971). Detection of a 40–50 day oscillation in the zonal wind in the Tropical Pacific. *Journal of the Atmospheric Sciences*, *28*(5), 702–708. https://doi.org/10.1175/1520-0469(1971)028<0702:DOADOI>2.0.CO;2

Mapes, B. E., & Houze, R. A. (1993). Cloud clusters and superclusters over the oceanic warm pool. *Monthly Weather Review*, *121*(5), 1398–1416. https://doi.org/10.1175/1520-0493(1993)121<1398:CCASOT>2.0.CO;2

Morcrette, C. (2013). *Sub-grid cloud parametrization issues in the met office unified model: A tale of several grey zones.*

Muller, C., & Bony, S. (2015). What favors convective aggregation and why? *Geophysical Research Letters*, *42*(13), 5626–5634. https://doi.org/10.1002/2015GL064260

Muller, C., & Held, I. M. (2012). Detailed investigation of the self-aggregation of convection in cloud-resolving simulations. *Journal of the Atmospheric Sciences*, *69*(8), 2551–2565. https://doi.org/10.1175/JAS-D-11-0257.1

Nakazawa, T. (1988). Tropical super clusters within intraseasonal variations over the Western Pacific. *Journal of the Meteorological Society of Japan*, *66*(6), 823–839. https://doi.org/10.2151/jmsj1965.66.6_823

Smagorinsky, J. (1963). General circulation experiments with the primitive equations I. The basic experiment. *Monthly Weather Review*, *91*(3), 99–164. https://doi.org/10.1175/1520-0493(1963)091<0099:GCEWTP>2.3.CO;2

Smith, R. N. (1990). A scheme for predicting layer clouds and their water content in a general circulation model. *Quarterly Journal of the Royal Meteorological Society*, *116*(492), 435–460. https://doi.org/10.1002/qj.49711649210

Vaquero-Martínez, J., Antón, M., Ortiz de Galisteo, J. P., Román, R., & Cachorro, V. E. (2018). Water vapor radiative effects on short-wave radiation in Spain. *Atmospheric Research*, *205*, 18–25. https://doi.org/10.1016/j.atmosres.2018.02.001

Walters, D., Baran, A. J., Boutle, I., Brooks, M., Earnshaw, P., Edwards, J., et al. (2019). The Met Office Unified Model Global Atmosphere 7.0/7.1 and JULES Global Land 7.0 configurations. *Geoscientific Model Development*, *12*(5), 1909–1963. https://doi.org/10.5194/gmd-12-1909-2019

Wilson, D. R., & Ballard, S. P. (1999). A microphysically based precipitation scheme for the UK Meteorological Office Unified Model. *Quarterly Journal of the Royal Meteorological Society*, *125*(557), 1607–1636. https://doi.org/10.1002/qj.49712555707

Wilson, D. R., Bushell, A. C., Kerr-Munslow, A. M., Price, J. D., & Morcrette, C. J. (2008). PC2: A prognostic cloud fraction and condensation scheme. I: Scheme description. *Quarterly Journal of the Royal Meteorological Society*, *134*(637), 2093–2107. https://doi.org/10.1002/qj.333

Wing, A. A. (2019). Self-aggregation of deep convection and its implications for climate. *Current Climate Change Reports*, *5*, 1–11. https://doi.org/10.1007/s40641-019-00120-3

Wing, A. A., & Cronin, T. W. (2016). Self-aggregation of convection in long channel geometry. *Quarterly Journal of the Royal Meteorological Society*, *142*(694), 1–15. https://doi.org/10.1002/qj.2628

Wing, A. A., & Emanuel, K. A. (2014). Physical mechanisms controlling self-aggregation of convection in idealized numerical modeling simulations. *Journal of Advances in Modeling Earth Systems*, *6*(1), 59–74. https://doi.org/10.1002/2013MS000269

Wing, A. A., Emanuel, K. A., Holloway, C. E., & Muller, C. (2017). Convective self-aggregation in numerical simulations: A review. *Surveys in Geophysics*, *38*(6), 1173–1197. https://doi.org/10.1007/s10712-017-9408-4

Wing, A. A., Reed, K. A., Satoh, M., Stevens, B., Bony, S., & Ohno, T. (2018). Radiative-convective equilibrium model intercomparison project. *Geoscientific Model Development*, *11*(2), 793–813. https://doi.org/10.5194/gmd-11-793-2018

Wing, A. A., Stauffer, C. L., Becker, T., Reed, K. A., Ahn, M.-S., Arnold, N., & Silvers, L. (2020). Clouds and convective self-aggregation in a multi-model ensemble of radiative-convective equilibrium simulations. *Journal of Advances in Modeling Earth Systems*, *12*(9), e2020MS0021380. https://doi.org/10.1029/2020MS0021380

Wood, N., Staniforth, A., White, A., Allen, T., Diamantakis, M., Gross, M., et al. (2014). An inherently mass-conserving semi-implicit semi-Lagrangian discretization of the deep-atmosphere global non-hydrostatic equations. *Quarterly Journal of the Royal Meteorological Society*, *140*(682), 1505–1520. https://doi.org/10.1002/qj.2235